SM Journal of Family Medicine ISSN: 2576-0262

Research Article

A Quadripartite Cu_2O-Cds-$Bivo_4$-WO_3 Visible-Light Driven Photocatalyst Contained Three Cascade Z-Scheme Systems: Focus on Conditions' Optimization, Scavenging Agents and the Mechanism Pathway Towards Sulfasalazine

Narges Omrani and Alireza Nezamzadeh-Ejhieh*

Department of Chemistry, Shahreza Branch, Islamic Azad University, Islamic Republic of Iran

Abstract

The explosive pollution of water suppliers via the discharged various industrial and pharmaceuticals effluents prompted researchers to construct novel adsorbents and photocatalysts, especially their visible-light driven photocatalysts. A novel coupled Cu_2O-CdS-$BiVO_4$-WO_3 quadripartite nanoscale catalyst was prepared and characterized by XRD, SEM-DX, x-ray mapping, and DRS techniques. Its pHpzc was also determined to be about 9. The Eg-values obtained were 1.95, 1.96, 2.16, 2.38, and 2.19 for Cu_2O, $BiVO_4$, CdS, WO_3, and quadripartite catalysts, respectively. The photodegradation experiments were designed via RSM. The significance of the suggested model was confirmed by greater model F-value of 26.19 than $F_{0.05,14,15}$=2.55. The optimal run in the photodegradation of sulfasalazine (SFSZ) included the CSFSZ: 7 mg/L, pH 6.25, 30 min irradiation time, 0.45 g/L of the catalyst dose, by a catalyst with a Cu_2O-CdS-$BiVO_4$-WO_3 mole ratio 3:1:1:1 under visible light illumination. The effects of the scavenging agents were also studied, and the results confirmed the critical role of superoxide in SFSZ photodegradation and the hydroxyl radicals. The photodegradation pathway obeyed the direct Z-scheme mechanism, which involved three successive binary Z-scheme components involving WO_3-$BiVO_4$, $BiVO_4$-CdS, and CdS-Cu_2O, which accumulates the photoinduced electrons in the CB-Cu_2O and the holes in the VB-WO_3, the more powerful reducing and oxidizing centers, respectively.

Keywords: Type II-heterojunction; Direct Z-scheme mechanism; Quadripartite catalyst; RSM; Antibiotics.

INTRODUCTION

In recent decades, various synthetic pharmaceutics have critically protected humans' lives and domestic animals from many diseases. This broad use accumulates them in the environment, especially aquatic ones, causing severe environmental implications such as bacterial resistance [1- 8]. Further, some pharmaceutics have high resistivity against the biodegradation, natural degradation, and photo-transformation processes [9-11]. Thus, due to the continuous discharge of chemical industries and disposal from consumers into the natural environment, their accumulation in the atmosphere is increasing. Accordingly, their environmental concentration reached a few mg to g per kg in soils and water. This is high enough to yield an unhealthy environment [12].

A combined sulfa drug sulfasalazine (SFSZ) consists of sulfapyridine and salicylate via an Azo bond. It became widely used to treat rheumatoid arthritis because of its antibacterial characteristics. SFSZ has a high persistence in the environment, and thus, it was subjected as a pollutant model here. Due to the frequent use and discharging of personal care drugs to the environment, removing them before discharging their corresponding effluents greatly diminishes their environmental accumulation and hazards [13].

However, more physical removal techniques transfer the subjected concomitant to another phase, requiring further secondary removal [14-18]. Thus, special attention has been paid to the advanced oxidation processes (AOPs) that commonly mineralize the pollutant used in some inert/harmless species [19-23]. The best efficient AOPs' technique is the heterogeneous semiconducting materials' based photocatalysis under the semiconductor illumination process by UV of visible photons with adequate photo energy ≥ semiconductors' band gap energy (Eg) [24-30]. The semiconductors' valence band (VB) electrons (e^-) can be excited to its conduction band (CB) under the illumination process, leaving holes (h^+) in the VB. These photoinduced e/h pairs can begin subsequent attacks on the molecules of the pollutant to degrade them [31,32]. They also can react with the dissolved oxygen and water molecules to produce the superoxide and hydroxyl radicals, respectively, as powerful oxidizing centers to attack the pollutant used [33-36].

The major problem with efficiency in heterogeneous photodegradation is the e/h recombination; thus, when it is relatively high, the overall efficiency of the process can be drastically low [37-39]. This drawback can be overcome critically by various techniques, including converting the semiconductor to nanoscale [40-48], supporting on various supports [49-52], coupling of two or more semiconducting materials, or construction of heterojunction systems or co-catalysts [53-64], doped systems with metals/non-metals species [65-68], vacancy engineering [22,69] etc. Thus, the coupling of nano-scale semiconductors was used to enhance the photocatalytic activity of Cu_2O, CdS, $BiVO_4$, and WO_3 in this work. In the coupled systems, charge carriers transfer between the VB and CB positions of the connected semiconductors, resulting a critical decreased e/h recombination process via various mechanisms such as type(II)

Submitted: 25 February, 2025 | **Accepted:** 07 March, 2025 | **Published:** 10 March, 2025

***Corresponding author:** Alireza Nezamzadeh-Ejhieh, Department of Chemistry, Shahreza Branch, Islamic Azad University, P.O. Box 311-86145, Shahreza, Islamic Republic of Iran.

Citation: Nezamzadeh-Ejhieh A, Omrani N (2025) How Community Pharmacists Can Make a Difference in Black Health: Black Bioethics and the Ethics of Empathy and Care . SM J Fam Med 3:3-23.

heterojunction, direct Z-scheme [70], and S-scheme pathways [70-73]. In the nano scale systems, the decreased path should be traveled by the charge carriers to reach the surface of the catalyst critically decreased, resulting in a decreased e/h recombination by the elongation of electrons and holes lifetimes. Unfortunately, the difficulty in the separation of nano scale catalysts from the suspensions has regarded as a drawback that can be covered by their excellent advantages like high effective surface area and lower e/h recombination rate.

The p-type Cu_2O semiconductor has a small band gap of 2 eV, while the n-type CdS and $BiVO_4$, about 2.4 eV and 2.5 eV are all visible light active photocatalysts [74]. The monoclinic $BiVO_4$ showed good photocatalytic activity in pollution removal and water splitting under simulated sunlight irradiation [74, 75]. The unique future of $BiVO_4$ is its VB constitution, which includes the coupling of the Bi 6s and O 2p orbitals. This destabilizes its electrons and acts as a driving force for upward excitation. Conversely, its coupled CB includes the V 3d, O 2p, and Bi 6p hybrid, causing a lower band. This is a significant factor in creating a direct band gap with a lower energy. Thus, despite most oxides, $BiVO_4$ can be excited under visible light illumination, resulting in a bright yellow color. Further, the coupled Bi 6s and O 2p VB orbitals improve the hole mobility, satisfying the photocatalysis process [76].

The p-type semiconductor with a direct band gap of about 2.5 eV is another visible light active photocatalyst. It is used as a sensitizer due to its absorption ability against photons of a large part of the visible region. The band edge positions of $BiVO_4$ CB and VB have been reported at 0.11 V and 2.65 V vs. NHE, while those of WO_3 at 3.3 V and 0.5 V vs. NHE, respectively. These values provide evidence of the possible formation of an n-p heterojunction between them, injecting the CB -$BiVO_4$ electrons to the CB -WO_3 to promote the e/h separation [77]. In general, in a coupled system including a large band gap semiconductor and a small band gap semiconductor with a more negative CB level, CB electrons of the small band gap material can transfer into the CB level in an extensive band gap material. Thus, this can happen between the narrow band gap $BiVO_4$ (with more negative CB) and WO_3 with a longer band gap, resulting in a higher photocatalytic activity of $BiVO_4$/WO_3 concerning the individual system [78].

We coupled Cu_2O, CdS, $BiVO_4$, and WO_3 and investigated the boosted photocatalytic activity of the obtained quadripartite photocatalyst in the photodegradation of sulfasalazine (SFSZ) in an aqueous solution. A brief characterization was done in the first part of the work [30], and the kinetics of the photodegradation and photomineralization processes were studied. Other characterization techniques were used to complete the work, and the optimal photodegradation process conditions were achieved using an experimental design optimization approach. Then, the effects of scavenging agents and the photodegradation mechanism were studied.

EXPERIMENTAL

Materials

The main chemicals used including $Cu(CH_3COO)_2.H_2O$ (>99%), $Bi(NO_3)_3.5H_2O$ (>99%), NH_4VO_3 (>99%), ammonium tungstate (>99%), NaOH (>95%), ascorbic acid (AA: $C_6H_8O_6$) (>99%), $CdNO_3$ (>99%), NH_4S (>99%), HNO_3 65%), etc., were analytical grade chemical prepared from Flucka/Aldrich Co. Sulfasalazine was prepared from Mehr Daru Co. IRAN, as a 500 mg pharmaceutical tablet. The pH of the aqueous solutions/suspensions (in distilled water) was adjusted by NaOH or HCl solution [79].

Preparations and synthesis

Each SFSZ tablet was 570.0 mg in weight, and thus, five tablets were thoroughly hand-mixed in a mortar, and 115.0 mg of the powder was added to 100 mL water. After 15 min stirring, it was filtered in a 250 mL volumetric flask and reached the mark with water. This solution was about 400 mg/L concerning SFSZ and used for diluter solutions [79].

Cu_2O NPs were obtained by dissolving 0.05 g copper acetate (0.27 mmole) in 100 mL water, followed by the addition of NaOH (0.2 g in 20 mL), under constant stirring for $Cu(OH)_2$ production. 15 mL aqueous solution of AA (0.39g/2.2m mole) was then added to convert Cu(II) to Cu(I) ($C_6H_8O_6$ was oxidized to $C_6H_6O_6$). At this moment, the deep blue color suspension was colorless, and a burgundy suspension was achieved, confirming Cu_2O colloid formation. It was centrifuged (>13000 rpm), and the solid Cu_2O was water washed three times and dried at 80°C [79,80].

To obtain CdS NPs, 100 mL 85 mM Cd(II) solution (as the nitrate salt), was prepared and slowly added to 100 mL 100 mM ammonium sulfide aqueous solution under a stirring speed of 1200 rpm. The stirring process was then continued for another 5 h. CdS NPs product was dark yellow, separated by centrifugation, washed with water, and air dried [79,81].

A hydrothermal synthesis procedure was used to synthesize $BiVO_4$ NPs: 20 mL concentrated nitric acid (65%) was added to 20 mmole bismuth nitrate to thoroughly dissolute it (solution A). Solution B was obtained by dissolving 20 m mole NH_4VO_3 in 20 mL 0.1 M NaOH. Dissolution of each solution A or B was completed under 2 h stirring. Then, solution A was added to B and stirred for 1 h to reach a stable homogeneous suspension. Its pH reached 7 and was transferred into a Teflon-lined stainless autoclave maintained at 180ºC for 6 h. The $BiVO_4$ NPs product (other products were N_2, NO_2, O_2, and H_2O), was separated and washed with water. The yellow $BiVO_4$ NPs were dried at 80ºC for 12 h [78,79].

Finally, WO_3 NPs were synthesized as below. 1.07 mmole (350 mg) $H_{42}N_{10}O_{42}W_{12}$-xH_2O was dissolved in 67 mL distilled water at 80ºC under vigorous magnetic stirring. After the droplet of 45 mL concentrated nitric acid was added, it was stirred (800 rpm) at 80ºC for 70 min. This remained at room temperature for a day to settle the WO_3 precipitate. After centrifugation, WO_3 was washed with water, dried at 80ºC, and calcined at 400°C for 70 min [79, 82].

The quadripartite Cu_2O-CdS-$BiVO_4$-WO_3 catalyst was prepared by hand-mixing the adequate weight of each component required to reach a definite mole ratio in an agate mortar for 30 min [79].

Characterizations

The samples prepared were characterized by the following techniques/instruments. A X'PertPro XRD diffractometer (Ni-filter, Cu-Kα source at 1.5406 Å, Acc. Voltage: 40 kV, i: 30 mA; Netherland), An UV–Vis diffuse reflectance spectrophotometer (JASCO V 670, reference: BaSO4, Japan), MIRA3LMU scanning electron microscope (TESCAN Co Czech Republic), a transmission electron Microscope Philips EM 208s (100 kV), a photoluminescence spectrophotometer (Perkin Elmer, LS 45, UK), A UV-Vis double beam spectrophotometer (UV/Vis 2100S, JASCO, power source: AC 220 V/50 Hz, quartz cells), a centrifuge instrument (Sigma, rpm: 13000, g: 15493), and a p-ion meter device (Jenway model 3505) [79].

Photodegradation experiments

A dark experiment for a 10 min string of the suspensions was done to reach the equilibrated adsorption/desorption. For a photodegradation run, 10 mL 10 mg/L SFSZ solution (pH 6.25)/0.4 g/L of the catalyst was irradiated against a 40 W W-lamp (located 10 cm above the cell). A homogeneous mass transfer during the illumination process was achieved under constant magnetic stirring. At the end of the illumination process, it was centrifuged, and the supernatant was transferred to the UV-Vis cell. The absorbance of the solution (A) at λ_{max}= 359 nm was recorded and compared to that of the blank SFSZ solution (Ao). The removed SFSZ was estimated as C/Co (corresponding to A/Ao) [79].

RESULTS AND DISCUSSION

Characterization studies

XRD patterns, morphology: The proposed quadripartite photocatalyst involves WO_3, $BiVO_4$, CdS, and Cu_2O components. This work is a continuation of previously published works where the activity of the individual, binary, and ternary systems of the four elements mentioned above was studied in the SFSZ photodegradation process. The results have been published; thus, some characterization and photodegradation results have been illustrated in detail in our published works [79,83-88].

As mentioned above, some characterization results of the sample have been discussed in the first section of the work [79]. XRD patterns confirmed that a Cu_2O cubic (CPDS# 65-3288) [21], a CdS hexagonal phase (JCPDS# 42-1411) [89], a monoclinic $BiVO_4$ phase (JCPDS card No. 14-0688) [78], and a cubic WO_3 phase (JCPDS file no. 46-1096) [78], were formed. Substituting the pattern data in the Scherrer [90], and Williamson-Hall models [91] got the average crystallite size of 27.8 and 22.5 nm for the quadripartite catalyst, respectively.

The morphology of the quadripartite catalyst has also been studied, and the SEM images discussed in the previous paper [79]. Some SEM images are also presented in Figure 1, which prove the presence of some cubes (Cu_2O and WO_3 NPs), some hexagonal relatively distorted (CdS NPs), and some nano-flakes or plate-like NPs ($BiVO_4$ species) in the catalyst. Applying the image-j software has confirmed the nano dimension for the catalyst species [79]. Elemental EXD analysis in X-ray mapping images has also confirmed the presence and homogeneous distribution of the constituent elements in the quadripartite catalyst [79].

Optical properties and VB/CB potential positions: Optical properties of the individual and coupled catalysts have also been evaluated by performing photoluminescence (PL) and UV-Vis spectroscopy, the results of which have been presented in the first section of the work [79]. The PL intensity was decreased in the quadripartite catalyst, confirming higher e/h separation occurred by coupling the semiconductors. Further, when the moles of the components were changed, the PL intensity changed. The sample's band gap energy (Eg) was estimated using the absorption wavelength edge obtained from the absorption spectra. The Eg-values obtained were 1.95, 1.96, 2.16, 2.38,

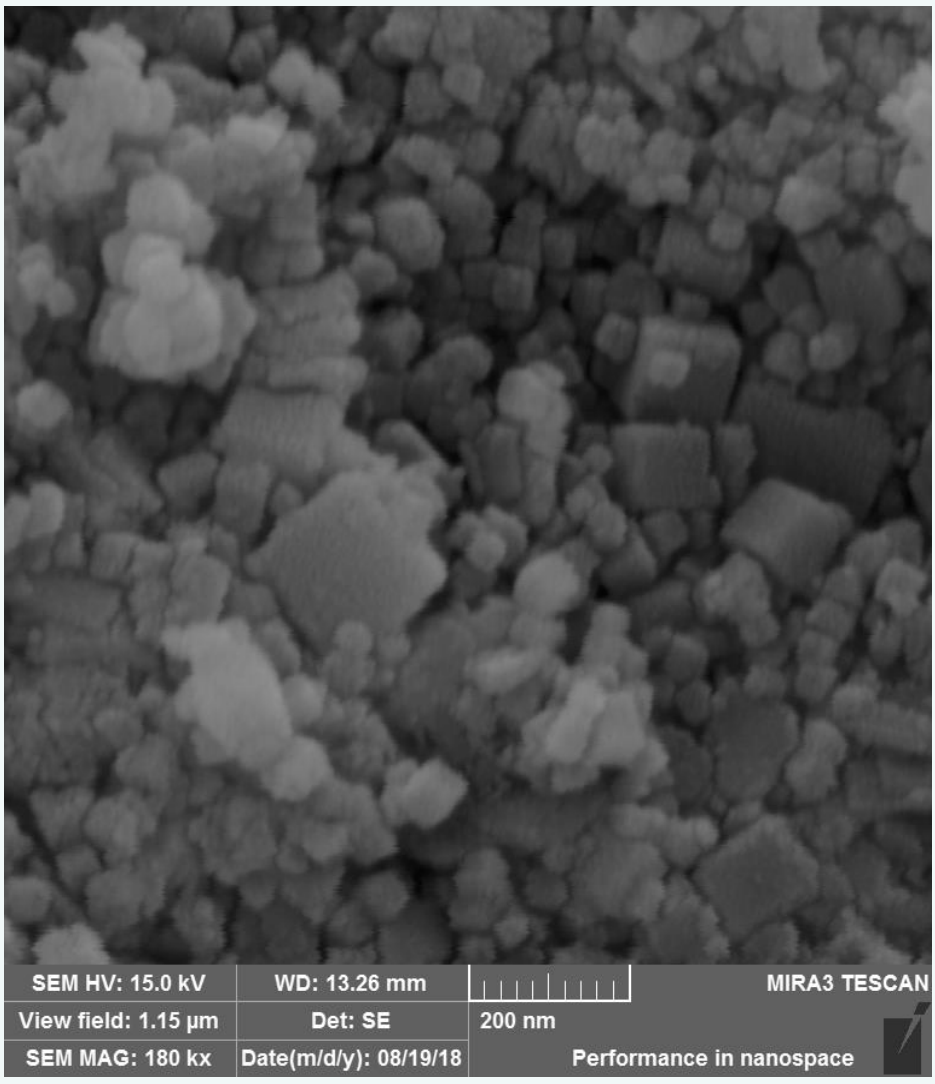

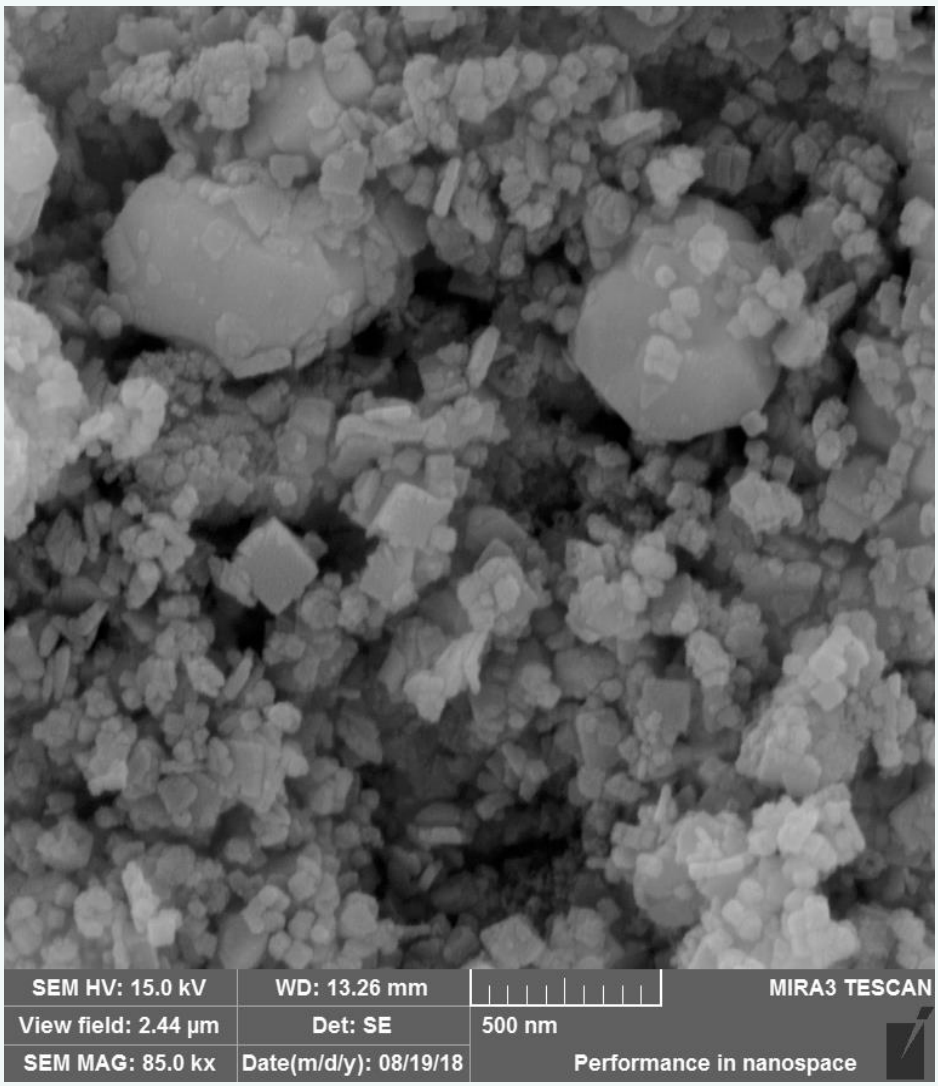

Figure 1: Some FESEM images of Cu2O-CdS-BiVO4-WO3 NPs (mole ratios 3:1:1:1) [79].

and 2.19 for Cu_2O, $BiVO_4$, CdS, WO_3, and quadripartite catalysts, respectively [79].

Here, we use the Kubelka-Munk and the Tauc models to estimate the more precise Eg-values based on the reflectance spectra of the samples [92-96]. In the Kubelka-Munk model, the Kubelka-Munk function ($F(R)=(1-R)^2/2R=K/S$) or the reflectance (R) can be converted into the absorption coefficient (α) [97] as follows. S and K are the scattering and absorption Kubelka-Munk coefficients [98].

$K = 2\alpha = SF(R)$

The Eg value for various electronic transitions can be estimated from the following Tauc relation:

$F(R)\ h\upsilon = A\ (h\upsilon - Eg)^n$

Depending on the type of transition that occurs, the power n gets various values. Depending on the electronic nature, the exponent n-vale gets values of 3, 2, 3/2, and 1/2 for the indirect forbidden (IF), indirect allowed (IA), direct forbidden (DF), and direct allowed (DA) transitions, respectively [99]. By the change in writing format for this equation, the n-value tends to change. For example, an n value equal to 1/2 for a direct band gap material is subjected to the above-mentioned formula. This equation can be rewritten for this direct electronic transition, and an n value of 2 must be achieved. In the following formula, an n value of 2 is for a DA transition, a value of 1/2 is for an IA transition, a value of 2/3 is for a DF transition, and a value of 1/3 is for an IF transition [100].

$(F(R)\ h\upsilon)^n\ \ A\ (h\upsilon - Eg)$

Due to s-d and p-d exchange interactions, a red shift in the band gap energies has been reported [101].

In the following format, n values of 1/2, 3/2. 2, and 3 show the DA, DF, IA, and IF transition, respectively [102-104].

$(\alpha h\upsilon)^{1/n} = A\ (h\upsilon - Eg)$

We can write the following model: the exponent n = 2 is for DA transition, n = 2/3 for DF transition, n = 1/2 for IA transition, and n = 1/3 for IF transition [105, 106].

$(\alpha h\upsilon) = A\ (h\upsilon - Eg)^{1/n}$

If the equation is written as follows, n gets values of 1, and 4, for DA and IA transitions, while the values of 3 and 6 for DF and IF transitions, respectively [107].

$(\alpha h\upsilon) = A\ (h\upsilon - Eg)^{n/2}$

This formula can construct a plot of ln $(\alpha h\upsilon)$ vs. ln $(h\upsilon - Eg)$ with an approximate Eg-value. The slope of a straight line gives the value of n for the transition investigated. For calculating the Eg-value, a plot of $(\alpha h\upsilon)^{2/n}$ vs. $h\upsilon$ should be constructed, providing a tangential line. This line is near the band edge. The extrapolation of the rising slope of the curve towards the x-axis of the photon energy, the obtained x-intercept is equal to the optical band gap [107].

Finally, in another format of the Kubelka-Munk equation, n values of

$(\alpha h\upsilon)^{2/n} = A\ (h\upsilon - Eg)$

Based on the reflectance data (Figure 2A), the Tauc plots were

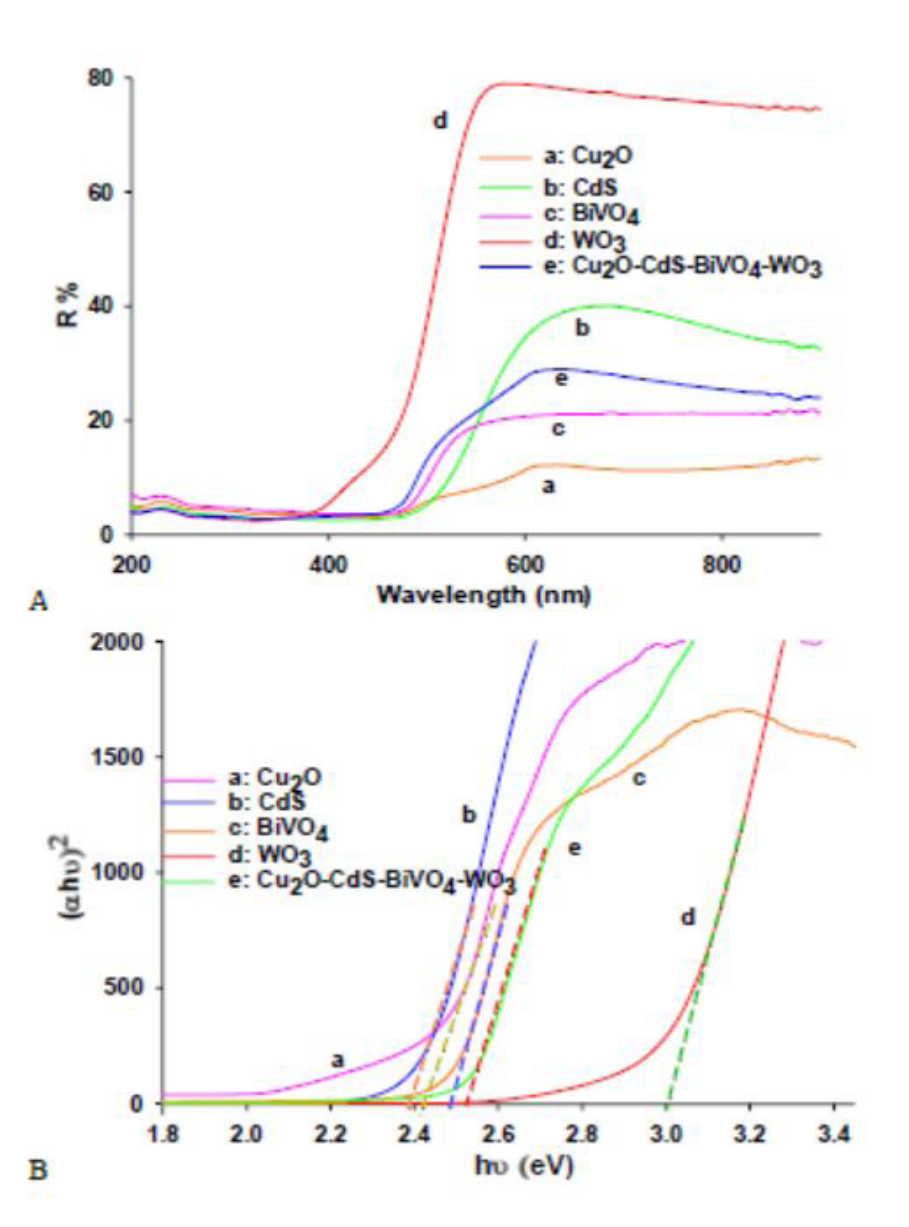

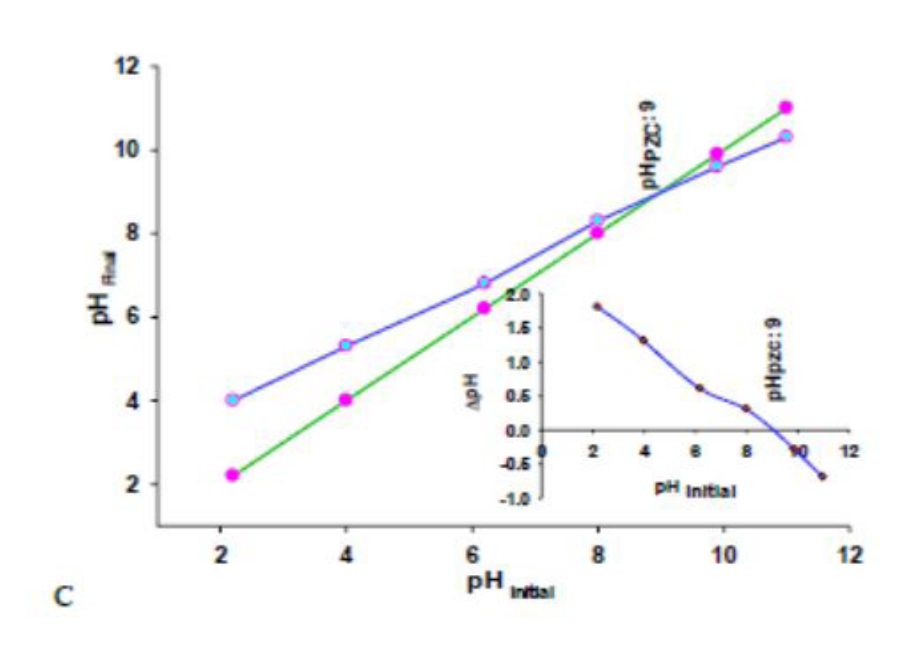

Figure 2: (A) Typical UV–Vis reflectance spectra obtained in DRS study of the Cu_2O, CdS, $BiVO_4$, WO_3 NPs and Cu_2O-CdS-$BiVO_4$-WO_3 quadripartite sample (mole ratios 3:1:1:1); **(B)** Typical Tauc plot for n= 2 obtained based on reflectance spectra in case A; **(C)** Typical plots for calculation of pHpzc of Cu_2O-CdS--$BiVO_4$-WO_3 [79].

constructed as shown in Figure 2B and SDF1 (supplementary data). As shown in Figure 2B, WO_3 NPs showed the most significant Eg, which can be lowered effectively when coupled with other semiconductors. The results obtained are summarized in Table 1, confirming that the as-synthesized catalysts are visible light active. The band gap energies for $BiVO_4$ and WO_3 NPs synthesized here showed a blue shift concerning the commercial $BiVO_4$ (Eg= 2.3 eV) and commercial WO_3 (Eg= 2.6 eV) due to the increased Eg in nanoscale [76].

In the next step, the catalyst's VB and CB potential positions were calculated by the following formulas: the free electrons energy is about 4.5 eV (vs NHE), and χ is the semiconductors' electronegativity [108]. This calculation illustrated the reasons for the increased separation rate of the photoinduced e/h pairs.

$$E_{CB} = \chi - E^e - 1/2\ Eg$$

$$E_{VB} = E_{CB} + Eg$$

The χ value of each semiconductor is a geometric mean of the electronegativity of each constituent element. As shown in Table 1, the atoms' electronegativity can be estimated from the atom's first ionization and electronegativity energies.

pHpzc: Exposing some metal oxides to the external environment, especially aqueous ones, changes the surface characteristics, significantly the accumulated surface charge. This is based on the proton balance between the solid surface and the aqueous suspension prepared, and the equilibrium adsorption/desorption reached would be expected to be forced by their acid-base futures. Commonly, the surface hydroxyl groups of the metal oxide can alter the surface electrical charges in an aqueous environment [42,109]. In general, the electrolyte concentration, pH, and the native properties of the solid material used can change the type of accumulated charges on the surface. This pH dependency of the surface charge of mineral adsorbents/ catalysts in an aqueous phase is critical in the overall process yield. Thus, to obtain more reliable optimal conditions for running the process, it is essential to know about the accumulated surface charge [110].

A critical pH point for describing the surface accumulated charge is the zero charge (pHpzc or PZC), in which the surrounding solution neutralizes the surface accrued charge. An equal number of de-protonated negative surface centers must balance the positive surface centers (via the protonation process). In general, knowing the pHpzc point of the sample used is very important, and it has been reported that the chemical properties of some soil samples and mineral oxides or hydroxides can be determined by their pHpzc future. The PZC characteristics played a critical role in the overall efficiency of some processes, such as ore flotation, adsorption of colloidal particles on the surface, etc. Further, the deposition efficiency of the corrosion products in steam generators and the transporting radioactivity efficiency in a water-cooled nuclear reactor can be illustrated by the pHpzc of the surface subjected [110].

Typical plots for determining the pHpzc of the quadripartite catalyst are shown in Figure 2. Before the pHpzc, the native basic or negative surface could adsorb protons from the adjacent aqueous phase, resulting in net positive surface charges and increase in the suspension pH (please focus on Figure 2). Beyond the pHpzc, the native acidic or positive future of the surface adsorbs hydroxyl anions from the adjacent aqueous media, resulting in a net negatively surface charge and a decreased suspension pH. The quadripartite catalyst showed a pHpzc around 9.

Photocatalytic studies

The boosted photocatalytic activity of the coupled system: Some preliminary removal runs were done to evaluate the capability of the quadripartite catalyst in SFSZ removal; which results have been discussed in the first section of the work [79]. The results are also shown in Figure 3. Briefly, a dark experiment for 10 min was done to achieve an equilibrated surface adsorption/desorption process [111], based on the preliminary experiments illustrated in the first part of the work. Then, the photodegraded solutions were compared against the direct photolyzed solution to obtain a net photodegradation efficiency.

Table 1: Band gap and potential positions for CB and VB of the semiconductors used.

Approximated band gap energies of the used catalysts by using the absorption edge method and Kubelka-Munk equation and Tauc plots						
Catalysts	**Tauc plots (eV)**				**Absorption edge**	
	1/2	**2**	**3/2**	**3**	**λ (nm)**	**Eg (eV)**
Cu_2O	2.665	2.412	2.445	2.425	636	1.949
CdS	2.667	2.382	2.489	2.487	573	2.164
$BiVO_4$	2.389	2.43	2.508	2.519	566	2.190
WO_3	2.820	2.998	3.011	3.027	634	1.955
Composite	2.453	2.523	2.549	2.562	520	2.384
E_a and E_i values of the constituent elements of the used semiconductors						
	Element	**E_a (eV)**	**E_i (eV)**	**½(E_a+E_i) (eV)**		
	Cu	1.235	7.712	4.475		
	O	1.461	13.618	7.539		
	Cd	0.724	8.985	4.854		
	S	2.077	10.358	6.217		
	Bi	0.942	7.238	4.090		
	V	0.527	6.739	3.633		
	W	0.816	7.864	4.340		
Eg, V_B and C_B values of the used semiconductors, χ data are in Mulliken's electronegativity scale						
	Catalyst	**χ (eV)**	**Eg (eV)**	**E_{VB} (eV)**	**E_{CB} (eV)**	
	Cu_2O	5.35	2.41	2.05	-0.36	
	CdS	5.49	2.38	2.18	-0.20	
	$BiVO_4$	6.02	2.43	2.73	0.30	
	WO_3	6.56	2.99	3.55	0.56	
Various formats for the Tauc model						
		n-value for:				
Formula		IF	IA	DF	DA	Ref.
$F(R)\ h\upsilon\ \ A\ (h\upsilon - Eg)^n$		3	2	3/2	1/2	[99]
$(F(R)\ h\upsilon)^n = A\ (h\upsilon - Eg)$		1/3	1/2	2/3	2	[101]
$(\alpha h\upsilon)^{1/n} = A\ (h\upsilon - Eg)$		3	2	3/2	1/3	[103, 134, 135]
$(\alpha h\upsilon) = A\ (h\upsilon - Eg)^{1/n}$		1/3	1/2	2/3	2	[105, 106]
$(\alpha h\upsilon) = A\ (h\upsilon - Eg)^{n/2}$		6	4	3	1	[107]
$(\alpha h\upsilon)^{2/n} = A\ (h\upsilon - Eg)$		6	4	3	1	[107]

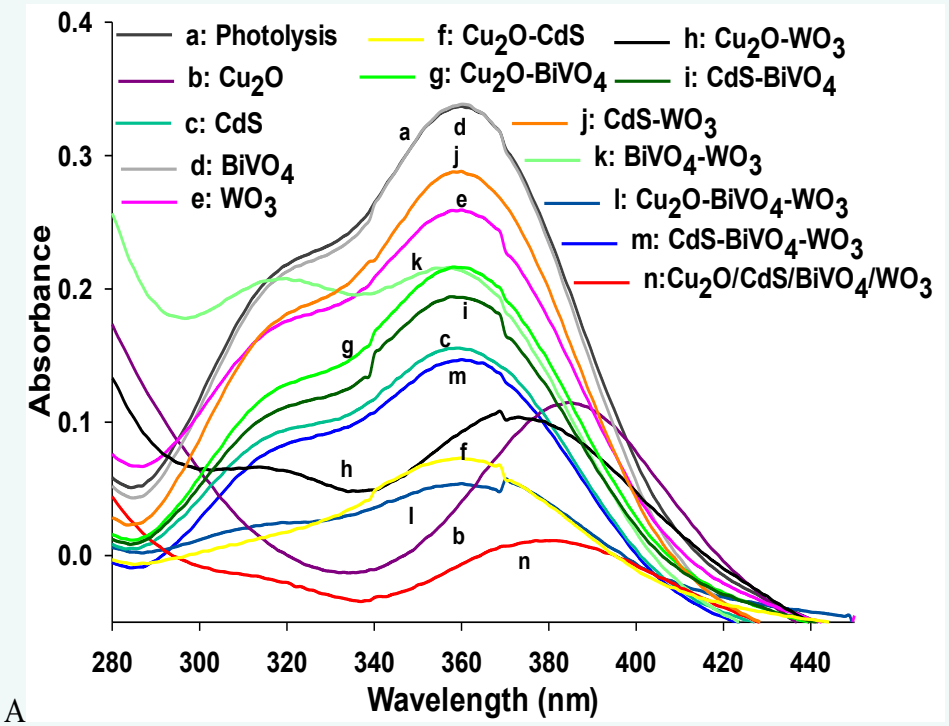

A

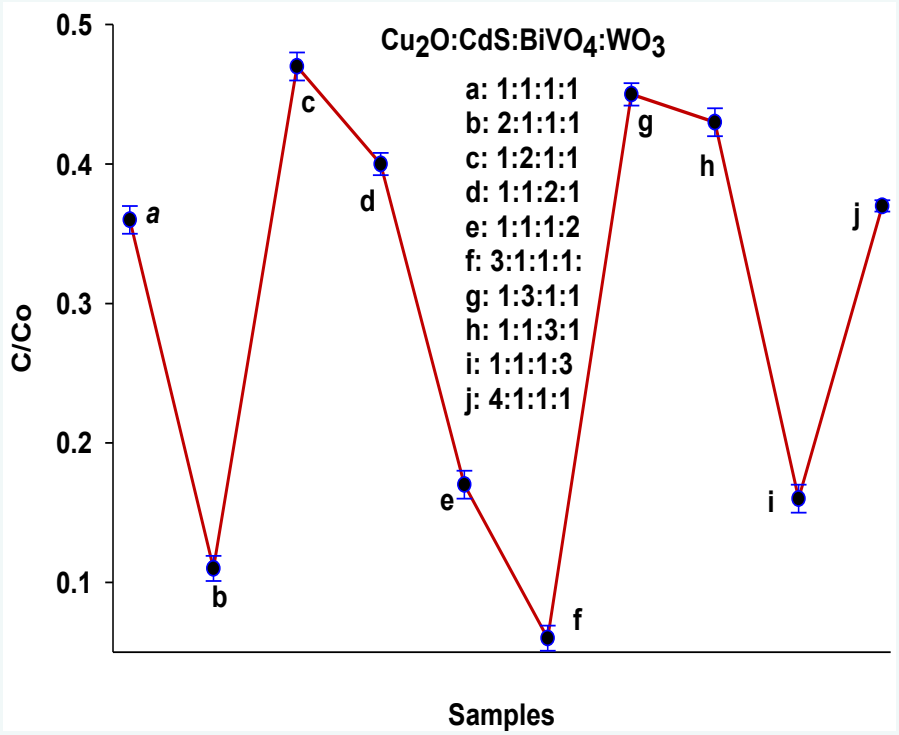

B

Figure 3: (A) Effects of direct photolysis and photocatalytic processes on SFSZ removal (catalysts dose 0.4 g/L, C_{SFSZ}: 10 mg/L, irradiation time: 30 min, initial pH 6.5); **(B)** Effects of the mole ratio of the Cu_2O:CdS:$BiVO_4$:WO_3 in photodegradation of SFSZ [79].

Based on the decrease in the peak intensity of the photodegraded solutions, the photodegradation efficiencies of 6, 27, 39, and 48% were achieved for $BiVO_4$, WO_3, CdS, and Cu_2O NPs in SFSZ photodegradation when used alone. This efficiency was enhanced to about 64% when the coupled quadripartite catalyst was used. This boosted effect is related to the faster separation of the photoinduced e/h pairs, which will be discussed in detail in the following sections by constructing suitable schematics. Based on the results [79], the change in the mass ratio of the components of the quadripartite catalyst, changed the PL intensity and the photodegradation efficiency. The lowest PL intensity and the highest photocatalytic activity were obtained when the quadripartite catalyst with a Cu_2O: CdS: $BiVO_4$:WO_3 mole ratio of 3:1:1:1 was used. In general, both the higher extent of the production of the e/h pairs and their lower recombination extent determine the overall efficiency of the process. These can be change by varying the semiconductor components in the catalyst, reached the optimal extents in the above-mentioned ratio [112]. Thus, this catalyst was used in the experimental design optimization approach to optimize the SFSZ photodegradation condition. The results will be discussed in the next section.

Experimental design (RSM) studies: Table 2 summarizes the selected influencing variable in the RSM study of SFSZ photodegradation process. The selected ranges include the axial level (±2), the cubic level from the factorial design (±1), and the central level (with a code of 0). Based on the selected ranges for each variable, a central composite design (CCD) was constructed by inputting the ranges to the software, which resulted in the suggestion of conditions for 30 runs (16 factorial (2^4), 8 axial (2k, k = number of factors), and 6 center point replicates). The coded values were obtained by the following formula: the coded and actual values of the independent variable (X_i and X_j) are X_{ci} and X_j, while its actual value at the center point is Xo. ΔX is the value of the step change [113].

$$x_{ci} = \frac{(Xi - Xo)}{\Delta X} \quad 0$$

After performing the photodegradation experiments based on the RSM runs' conditions, the viable response Y (SFSZ photodegradation%) was inputted into the software. The coefficients (β_0: the constant intercept, βi, βii, and βij: the linear, second order, and interactive effects regression coefficients, respectively) of the following quadratic (second order) were determined as shown in equation (2) [113, 114].

$$Y = \beta_0 + \sum\beta_i x_i + \varepsilon = \beta_0 + \sum\beta_i x_i + \sum\beta_{ii} x_i^2 + \sum\beta_{ij} x_i x_j + \varepsilon \quad (2)$$

$$Y\ (\text{Deg. }\%) = 28.68 - 3.82\ A - 11.83\ B + 13.57\ C + 0.43\ D - 3.33\ AB - 2.92\ AC + 0.81\ AD - 5.24\ BC + 3.32\ BD + 12.20\ CD - 0.51\ A^2 + 8.99\ B^2 + 3.79\ C^2 - 2.55\ D^2 \quad (3)$$

1. ANOVA and Fit summary: Other data in Table 2 belong to the ANOVA (analysis of the variance) analysis constructed based on the Fischer test (F-test) analysis. The significance of the model suggested can be evaluated by comparison of the model F-value of 26.19 (a divide of model MS to that of residual) with the critical value of $F_{0.05,\ 14,\ 15}$=2.55. This larger calculated F-value confirms that the suggested model can significantly process more than 95% of the data obtained, and only less than 5% cannot be processed. The model lack of fit (LOF) estimates the random errors, and for a significant model, this term must be not significant. Here, the LOF F-value (a divide of its MS to that of pure error) is 2.04, smaller than the tabulated F0.05, 10, and $_5$= 8.79. This smaller calculated F-value confirms a non-significant LOF, proving that random errors influenced the data obtained [115, 116].

The correlation coefficients, including the multiple correlation coefficients R^2 (R^2= 0.9607), adjusted-R^2 (adj-R^2=0.9240) and predicted-R^2 (pred-R^2 = 0.8070) were achieved. All values are close to unity, confirming a reasonable statistical data fit in the model [117].

A precision measure of the model can be evaluated by the CV (coefficient of variation) term, and a smaller CV value shows higher model precision. Here, a CV value of 7.20% was obtained, which is relatively low. Further, an adequate precision value of 19.80 was achieved, and in RSM, this value must be above 4 for a good model. This term estimates the S/N ratio in the space investigated or to navigate the design space [118].

2. Diagnostic plots: Diagnostic plots are shown in Figure 3A and SDF2. The normal probability plot in Figure 3 (A) confirms normal distribution of residual around the normal diagonal straight line with no trend. No transformation is required because no S-shaped curve was reached. The plot of residuals versus predicted response values tests the assumption of constant variance across the graph, which is confirmed by a random scatter.

As shown here, a typical plot of residuals versus an experimental run should show a random scatter to check the lurking variables that may influence the response variable during the experiment. The plot of actual responses versus the predicted responses detects a value or group of values the suggested model does not predict. This can be confirmed by a split of data points evenly by the 45-degree line.

3. Influencing plots: The influencing plots show the influence of individual runs, which are shown in Figure 3B and SDF3. Based on the externally studentized residual (outlier t, R-student) no outlier point is present because no data point is laid out of the control limits ±3. The outlier data points are not fitted well by the proposed model, due to a wrong value or model. The applicability of a definite data point to influence the model fit can be evaluated by the leverage–run plot, in which each run gets a numerical value between zero and one. A high leverage value near one proves the predicted and actual values have the same force with zero residual, which is terrible because an unexpected error source influenced the model.

The difference in fit can be evaluated by plotting DFFITS versus runs, and the value can be estimated by deleting the point and following the change in the fit. Thus, a larger DFFITS value proves more influence on the point in the fitted model. Mathematically, this is similar to the externally studentized residual with a high leverage point. The plot of Cook's distance versus runs measures the change in the regression when the case is deleted. Large values (2-3 times greater than the other points) commonly have high leverage and large studentized residuals; thus, these values must be re-investigated.

Finally, all diagnostic and influencing plots confirmed the goodness of the model suggested.

4. Model graph: 3D and related 2D contour plots are summarized in Figure 5 and SDF3 to present the simultaneous interactions between the binary variables investigated graphically. The suspension pH is a crucial experimental variable that critically influences the response. It simultaneously affects the accumulated charges on the catalyst's surface and the SFSZ molecules' ionic species. Depending on the pKa values of 2.4, 6.8, and 11 that have been reported for SFSZ salicylic ring, sulfonamide hydrogen, and azo bond or pyridine rings' nitrogen atoms, respectively [113], SFSZ molecules can be present as various ionic species depending the pH of the suspension.

Thus, it would be expected that at acidic pHs around 3.5, the sulfonamide hydrogen and the nitrogen atom of the azo bond or pyridine ring to be in the protonated form should be repelled by the positively charged surface of the catalyst (see pHpzc section). This negative effect can continue at pHs about 9, because the mentioned nitrogen atoms may be in the protonated form.

The concentration of the pollutant can change the collision probability between SFSZ molecules and the catalyst surface, where the reactive species with very short lifetimes are formed and absorb the arrived photons by the catalyst surface. Due to the lower collision probability at low concentrations, the reactive species may participate in the side reaction, resulting in photodegradation efficiency. The increased collision probability due to the increased concentration can increase

Table 2: Data used/obtained in the RSM study of SFSZ removal by the quadripartite Cu2O-CdS-BiVO4-WO3 catalyst.

Variables and surfaces for the design of experiment by RSM under CCD pattern					
Code/Factor	Unite	-1 level	+1 level	-α	+α
X1: **Contact time**	min	20	40	10	50
X2: **Ads. dosage**	mg/L	0.3	0.6	0.15	0.75
X3: C_{SFSZ}	mg/L	8	10	7	11
X4: pH	-	3.5	9	0.75	11.75
Analysis of variance (ANOVA) for %*degradation* of SFSZ					
Source	Sum Sq.	df	Mean Sq.	F value	p-value
Model	14412.82	14	1029.49	26.19	> 0.0001 **Sig.**
X1: time	4417.58	1	4417.58	112.36	<0.0001
X2: Ads. Dos.	4.39	1	4.39	0.11	0.0074
X3: $C_{pb(II)}$	3359.96	1	3359.96	85.46	<0.0001
X4: pH	22.44	1	22.44	3.31	0.0089
X1X2	2380.22	1	2380.22	60.54	<0.0001
X1X3	438.59	1	438.59	11.16	0.0045
X1X4	136.71	1	136.71	3.48	0.0082
X2X3	175.89	1	175.89	4.47	0.0052
X2X4	10.61	1	10.61	0.27	0.0061
X3X4	176.96	1	176.96	4.5	0.0509
$X1^2$	394.18	1	394.18	10.03	0.0064
$X2^2$	178.22	1	178.22	4.53	0.0502
$X3^2$	2218.48	1	2218.48	56.43	<0.0001
$X4^2$	7.25	1	7.25	0.18	0.6738
Residual	589.72	15	39.31		
Lack of Fit	473.66	10	47.37	2.04	0.2231 **not sig.**
Pure Error	116.06	5	23.21		
Cor Total	15002.54	29			
The results obtained for the applicability of the model					
Variable		Value/Type			
Optimized values		pH: 9, Dose: 0.45 g/L, time: 30 min, C_{SFSZ}: 6.25 mg/L			
Suggested model		Quadratic			
Predicted response		90.70			
95% CI low and high		86.6-95.0			
Predicted Std Dev		2.3			
Observed response (n=3)		95± 2.3			

A

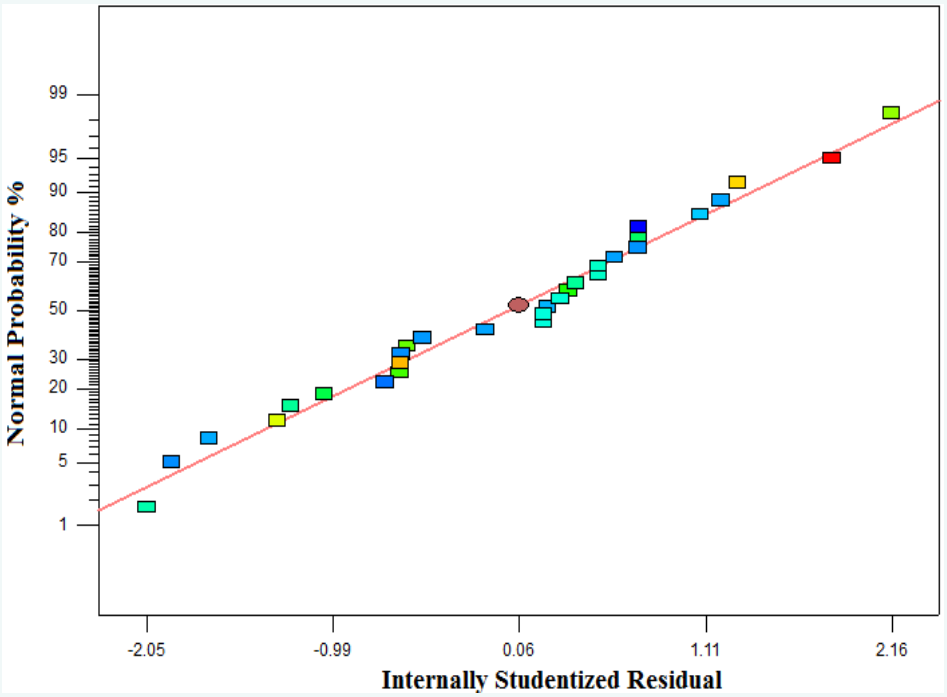

B

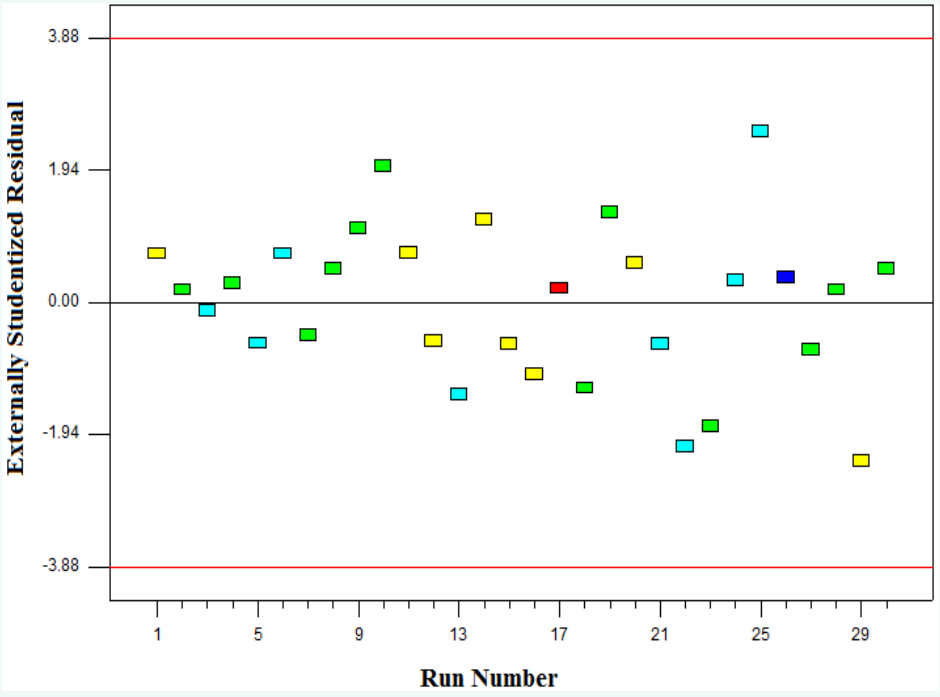

Figure 4: Typical diagnostic **(A)** and influencing **(B)** plots obtained in RSM study of SFSZ by Cu_2O-CdS-$BiVO_4$-WO_3 catalyst

A

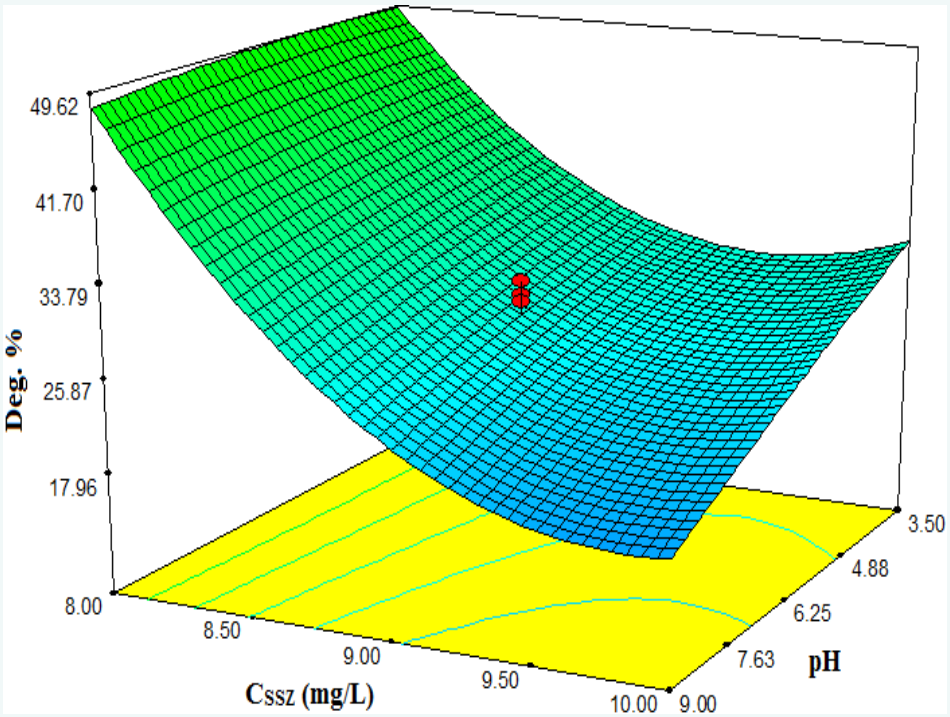
49.62
41.70
33.79
25.87
17.96
Deg. %
8.00
8.50
9.00
9.50
10.00
Cssz (mg/L)
3.50
4.88
6.25
7.63
9.00
pH

B

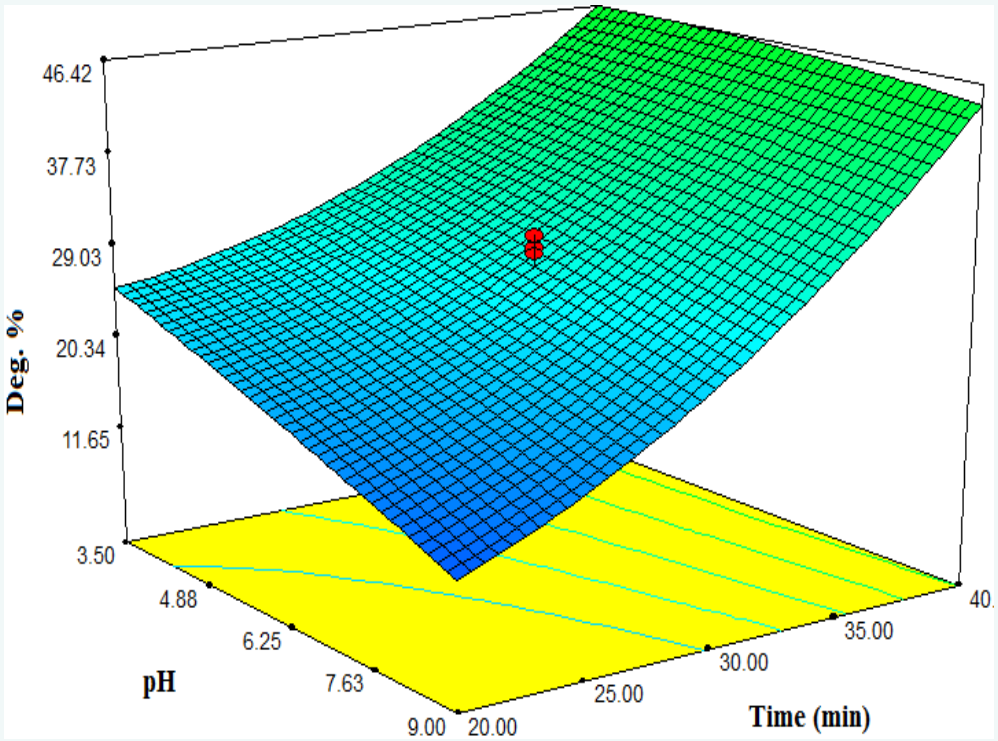
46.42
37.73
29.03
20.34
11.65
Deg. %
3.50
4.88
6.25
7.63
9.00
pH
20.00
25.00
30.00
35.00
40.
Time (min)

C

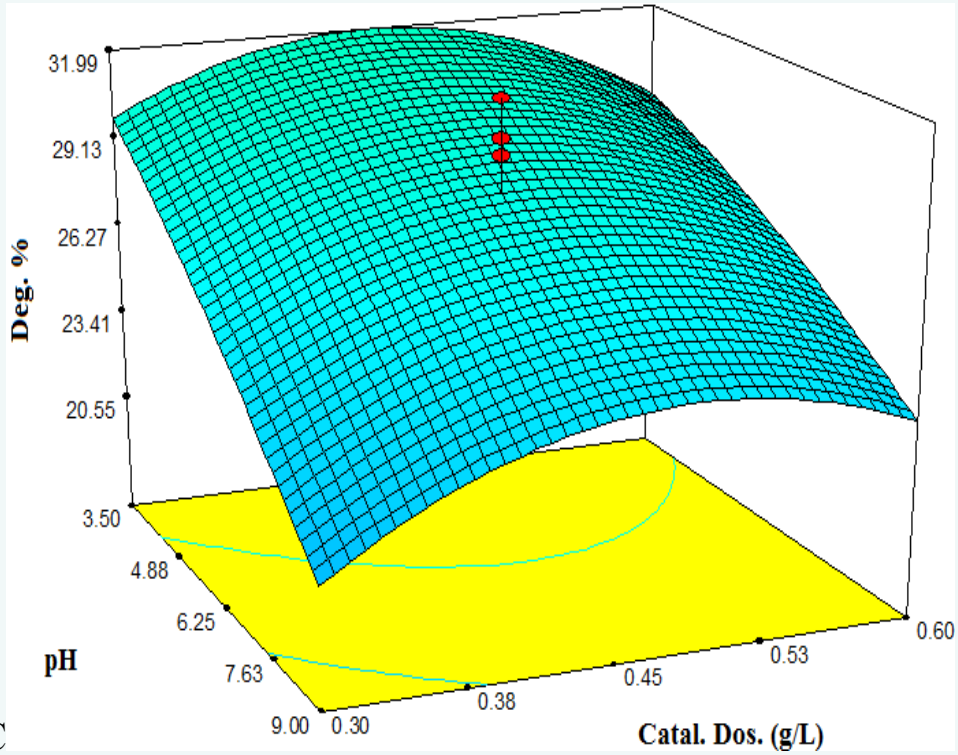
31.99
29.13
26.27
23.41
20.55
Deg. %
3.50
4.88
6.25
7.63
9.00
pH
0.30
0.38
0.45
0.53
0.60
Catal. Dos. (g/L)

D

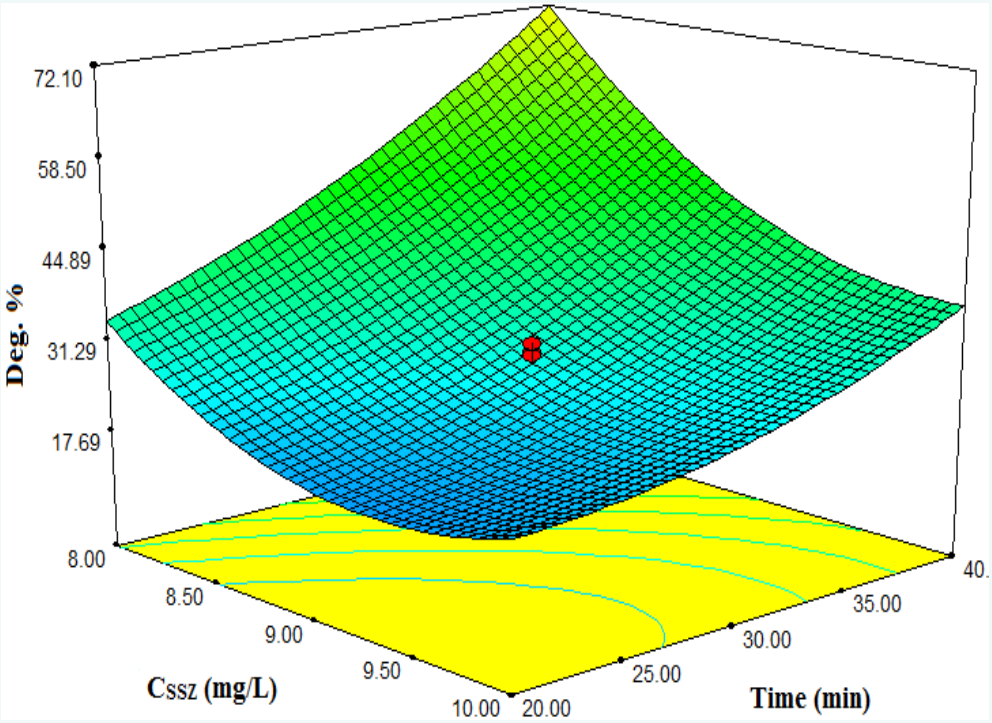
72.10
58.50
44.89
31.29
17.69
Deg. %
8.00
8.50
9.00
9.50
10.00
Cssz (mg/L)
20.00
25.00
30.00
35.00
40.
Time (min)

E

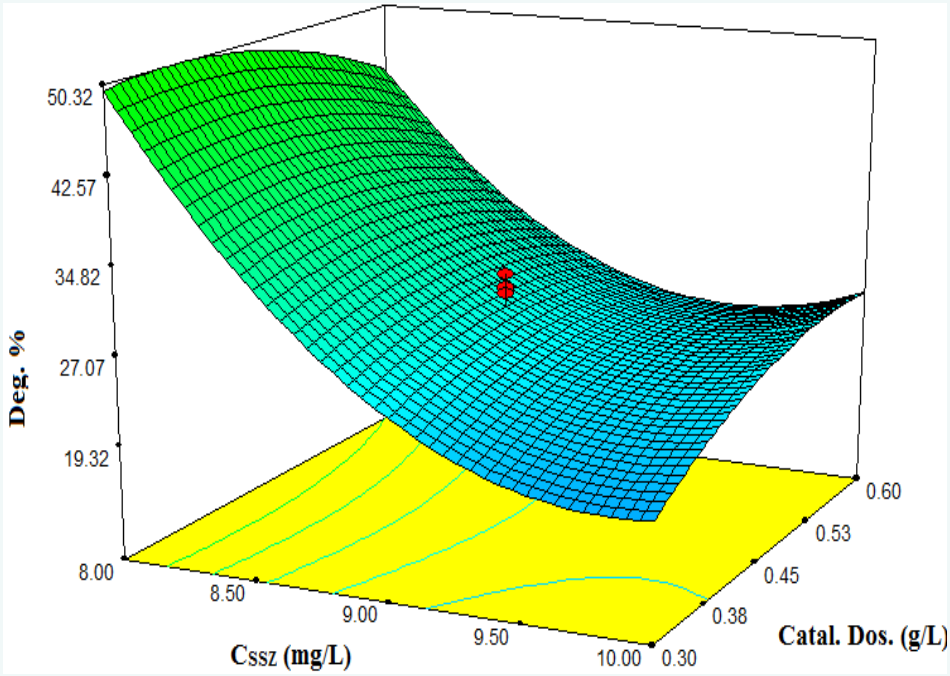

F

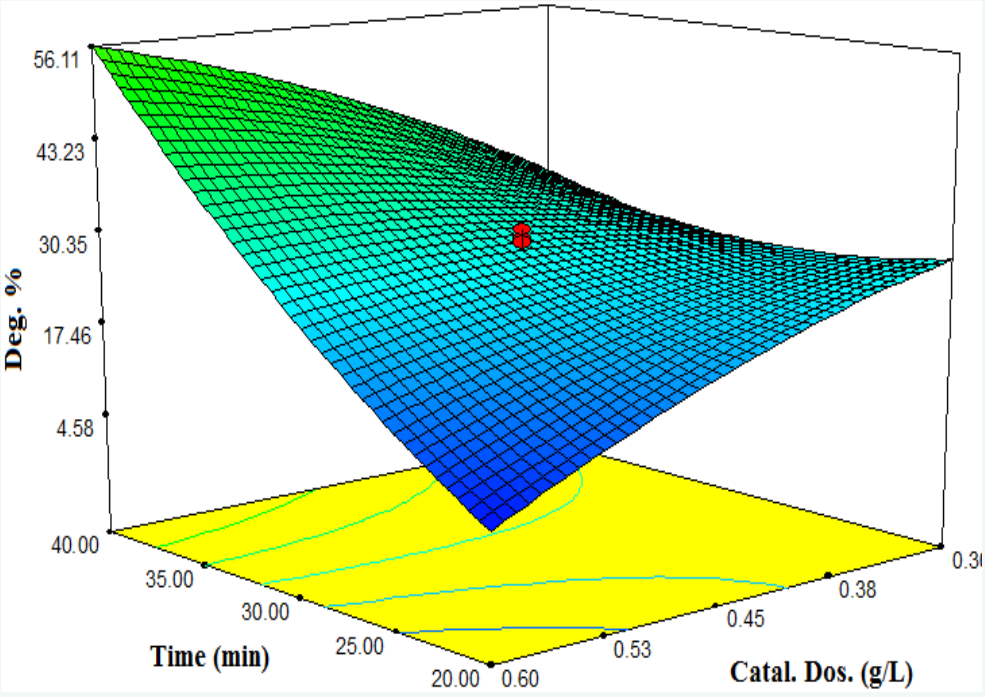

Figure 5: 3D response surface plots for effects of process variables on SFSZ by Cu_2O-CdS-$BiVO_4$-WO_3 catalyst.

the photodegradation efficiency. However, high amounts of the arrived photons may be absorbed in the high SFSZ concentration, adversely affecting the photodegradation of SFSZ molecules. Thus, an optimal concentration value would be expected. Thus, in Figure 5A, through the pH range of 3.5-9, the photodegradation efficiency cannot be increased at high concentrations, and the best optimal interactions between pH-C can be achieved at moderate concentrations of 8 ppm. Based on the results in Figure 5B, the negative effects of the pH range of 3.5-9 cannot be compensated by shorter irradiation times.

The catalyst dose can affect both the aggregation of the solid powder and the amounts of active centers to be illuminated. With mass increasing the catalyst, more active centers can be illuminated to produce the reactive species. At the same time, it aggregates the catalyst species and reduces the effective surface area under illumination. As shown in Figure 5C, a moderate dose of 0.45 g/L at more acidic pHs caused a better photodegradation efficiency. In this pH, the sulfonamide hydrogen may be released, and thus, an attractive force between this segment and the catalyst surface may attract SFSZ molecules and bring them near the surface to be degraded.

The interactions of C-Time in Figure 5D confirm that moderate concentrations of 8 ppm have better collision probability than 10 ppm, resulting in a more extended degradation yield. This confirms that some resist intermediates may form, needing longer illumination times to be degraded. The adverse effects of higher doses of the catalyst can be compensated by using relatively lower concentrations (Figure 5E), and longer irradiation times (Figure 5F).

The model's applicability was evaluated by performing SFSZ photodegradation runs in the optimal runs' conditions of pH 6.25, catalyst dosage 0.45 g L^{-1}, irradiation time 30 min, C_{SFSZ}: 7 g/L. The results were averaged based on triplicate measurements and compared with the acceptable range suggested by the model. Good agreement between them confirms the applicability of the proposed model in SFSZ photodegradation (Table 2).

Scavenging agent's effects and the photodegradation mechanism: As illustrated in the introduction section, in a typical heterogeneous photocatalytic process, the main reactive species of e^-, $^{\bullet}O_2^-$, h^+, and $^{\bullet}OH$ produced under the appropriate light irradiation are responsible for the degradation of various organic pollutants. To estimate their relative importance in the degradation reaction, the change in the photodegradation activity of the proposed quadripartite catalyst in the presence of $K_2S_2O_8$, $KHCO_3$, acetic acid, and ascorbic acid (AA) as the scavenging agents were followed. The proposed trapping agents can respectively trap the photoinduced electrons (e^-), hydroxyl radicals ($^{\bullet}OH$), photoinduced holes (h^+), and superoxide ion radicals ($^{\bullet}O_2^-$), respectively. Accordingly, the scavenging of each reactive species must decrease overall photodegradation efficiency, proving the higher role of the investigated reactive species in the photodegradation process. The photodegradation results are shown in Figure 6A. Peroxodisulfate (PDS), peromonosulfate and hydrogen peroxide, are known as electron scavengers in the heterogeneous photocatalytic process. During this scavenging process, PDS production is sulfate anion radicals ($SO_4^{\bullet-}$). Following rate constants have been reported for PDS and sulfate radicals contained reactions in acidic pH range of 3-8 [119].

$$S_2O_8^{2-} + \text{Heat} \rightarrow 2\,SO_4^{\bullet-} \qquad (k_1: 5.7 \times 10^{-5}\ s^{-1})$$

$$SO_4^{\bullet-} + S_2O_8^{2-} \rightarrow S_2O_8^{\bullet-} + SO_4^{2-} \qquad (k_2: 6.1 \times 10^{-5}\ M^{-1}\ s^{-1})$$

$$SO_4^{\bullet-} + H_2O \rightarrow {\bullet}OH + H^+ + SO_4^{2-} \qquad (k_3\ [H_2O] < 2 \times 10^{-3}\ M^{-1}\ s^{-1})$$

$$SO_4^{\bullet-} + SO_4^{\bullet-} \rightarrow S_2O_8^{2-} \qquad (k_4: 5 \times 10^{8}\ M^{-1}\ s^{-1})$$

The powerful •OH for photochemical decontamination in freshwater can be photochemically generated by illuminating nitrate, nitrite, and dissolved organic matter (DOM). Simultaneously, many solutes, such as DOM itself, can scavenge these radicals and inorganic carbon as carbonate and bicarbonate salts. The scavenging reaction kinetics of $^{\bullet}OH$ and carbonate or bicarbonate obeys a second-order model with rate constants of $3.9 \times 10^8\ M^{-1}\ s^{-1}$ and $8.5 \times 10^6\ M^{-1}\ s^{-1}$, respectively. The produced $CO_3^{\bullet-}$ is less reactive than $^{\bullet}OH$ [120].

Acetic acid is known as an effective hole scavenger [121]. Ascorbic acid undergoes the one or two electron steps redox reactions that form semidehydroascorbic acid and dehydroascorbic acid (DHA + $2H^+$ + $2e^-$ → ASC + H_2O, E^o (pH 7) = 60 mV) [122]. AA is a superoxide radical scavenger, and in the presence of acetaldehyde and xanthine oxidase (as the superoxide radical sources), the second order rate constant of $8{\cdot}2 \times 10^7\ M^{-1}s^{-1}$ has been reported for the scavenging of superoxide by AA. Another first-rate constant for such scavenging reaction has been reported as $2{\cdot}7 \times 10^5\ M^{-1}s^{-1}$ (in the presence of a xanthinexanthine oxidase system) [123].

As depicted in Figure 6A, the inhibition trend is as ascorbic acid > acetic acid > $KHCO_3$ > $K_2S_2O_8$, proving that the critical photodegradation role by the proposed catalyst belongs to the photogenerated $^{\bullet}O_2^-$ and then to $^{\bullet}OH$. The results show that the photoinduced e^- and h^+ species play a minor role during the photodegradation reaction. Based on the results obtained here and using the VB/CB potential positions obtained in DRS section, the photodegradation mechanisms were proposed, which will be discussed in the following.

So far, various mechanisms have been described to illustrate the photodegradation pathways in heterogeneous photocatalysis. These mechanisms involve direct Z-scheme photocatalysts, traditional Z-scheme photocatalysts, all-solid-state Z-scheme photocatalysts, type II-heterojunction systems, etc. [124-126].

In heterojunction systems, the Type- photocatalytic mechanism is usually the most common. This mechanism is shown in Figure 6B when the coupled semiconductors are considered successive binary heterojunction systems. Under the visible light irradiation of the system, all components can be excited to produce the e/h pairs. Among the CB positions, the CB-Cu_2O has a more negative (higher) potential position (-0.36 V) than that of CB-CdS (-0.28 V), satisfying the electron transfer from CB-Cu_2O to CB-CdS direction. Consequently, the CB-CdS electrons can rapidly transfer to that of the CB-$BiVO_4$ position with a more positive potential position (0.3 V). The final goal of these electrons is the CB-WO_3 position with the most possible position (0.36 V) among all CB positions involved.

Meanwhile, the photogenerated holes' transfer obeys a reverse path from the VB-WO_3 (3.55 V) to VB-$BiVO_4$ (2.73 V), then to VB-CdS (2.73 V) and finally to VB-Cu_2O (2.05 V). Overall, these e/h migrations result in the accumulation of the photogenerated electrons in the CB-WO_3 (0.56 V) and the holes in the VB-Cu_2O (2.05 V). These successive reduction/oxidation steps between the coupled components promote the spatial separation of the photoinduced e/h pairs, resulting in a suppressed recombination for the photoinduced e/h charge carriers. Overall, this quadripartite catalyst can be considered as three type(II)-heterojunction component involving the WO_3-$BiVO_4$, $BiVO_4$-CdS, and CdS-Cu_2O. On the other hand, this system can be regarded as a typical cascade type(II) heterojunction system in which the above mentioned binary type(II) heterojunction systems are consequently connected.

This suggested type (II) heterojunction system is not capable of producing sufficient superoxide radicals because the accumulated CB-WO_3 electrons with a very positive potential position (E: 0.56 V) concerning that of oxygen reduction (E: -0.28 V), cannot reduce the dissolved oxygen to superoxide radicals. In this suggested mechanism, only superoxide radicals can be produced by the electrons in the CB-Cu_2O, which is relatively free from the photogenerated electrons due to the successive migrations towards CB-WO_3. Similarly, the difference in the potential positions of the photoaccumulated hole in the VB-Cu_2O (E: 2.05 V) and that of water oxidation to produce hydroxyl radicals (E: 2.35 V) is tiny to the effective production of enough hydroxyl radicals. This proposed

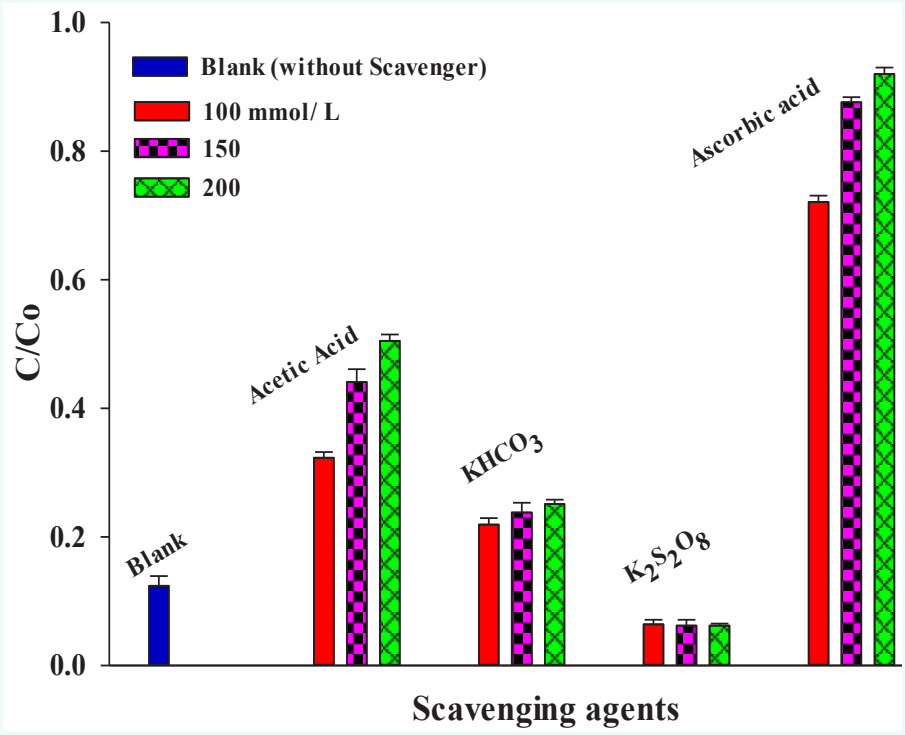
1.0
0.8
0.6
0.4
0.2
0.0
C/Co
Blank (without Scavenger)
100 mmol/ L
150
200
Blank
Acetic Acid
KHCO3
K2S2O8
Ascorbic acid
Scavenging agents

A

B

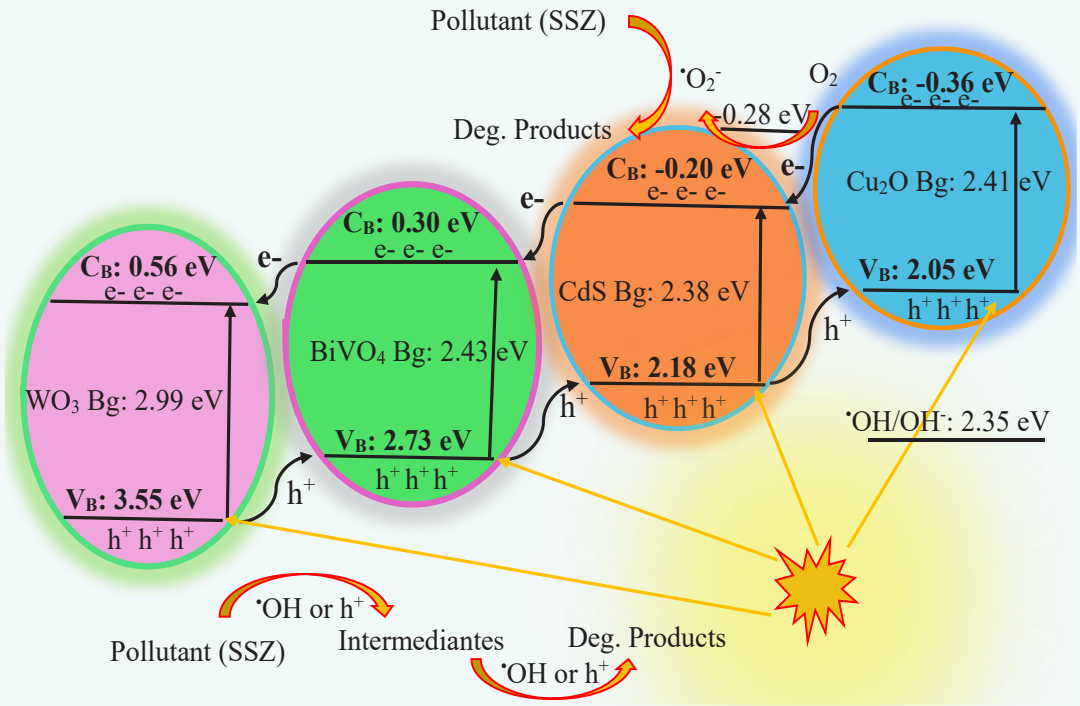
Pollutant (SSZ)
•O2-
O2
-0.28 eV
Deg. Products
CB: -0.36 eV
e- e- e-
Cu2O Bg: 2.41 eV
VB: 2.05 eV
h+ h+ h+
CB: -0.20 eV
e- e- e-
e-
e-
CB: 0.30 eV
e- e- e-
BiVO4 Bg: 2.43 eV
VB: 2.73 eV
h+ h+ h+
CB: 0.56 eV
e- e- e-
WO3 Bg: 2.99 eV
VB: 3.55 eV
h+ h+ h+
CdS Bg: 2.38 eV
VB: 2.18 eV
h+ h+ h+
h+
h+
h+
•OH/OH-: 2.35 eV
•OH or h+
Pollutant (SSZ)
Intermediantes
Deg. Products
•OH or h+

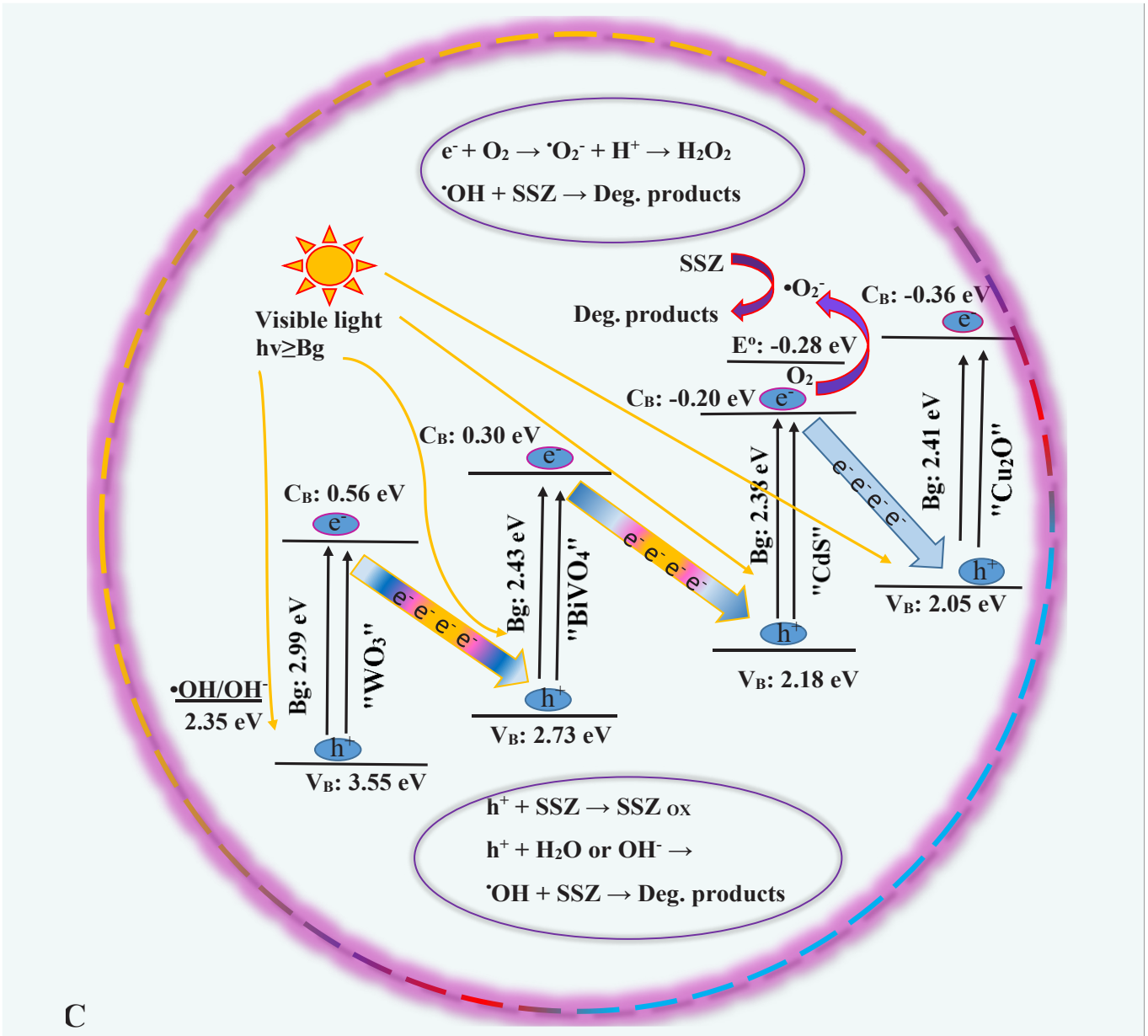

Figure 6: (A) Effects of some scavenging agents in SFSZ photodegradation (catalysts dose g/L, C_{SFSZ}: mg/L, irradiation time: min, initial pH); **(B-C)** Proposed mechanism for SFSZ photodegradation by the proposed Cu_2O-CdS-$BiVO_4$-WO_3 photocatalysts

successive type II-heterojunction charge transfer pathway for the proposed quadripartite catalyst is unsuitable for producing enough superoxide and hydroxyl radicals under the illumination process. Furthermore, if direct degradation of SFSZ molecules by the photoinduced electrons is considered a type of SFSZ degradation, its efficiency is also low. The direct oxidation potential of SFSZ molecules has been reported to be about 0.75 V [127], and its difference with that of CB-WO_3 is about 0.2 V. Thus, SFSZ cannot be degraded effectively (reduced) by the photoaccumulated CB-WO_3 electrons.

Thus, we considered another charge carrier transfer pathway to illustrate the excellent SFSZ degradation efficiency obtained by the proposed photocatalyst based on the results obtained in the study of scavenging agents. The direct Z-scheme photocatalysts are patterns like natural photosynthesis systems with outstanding merits of high light harvesting, critical spatially separated reductive and oxidative active centers, and a well-preserved powerful redox characteristic. Thus, such a system has been widely used in photocatalysis, photodegradation, water splitting for O_2 and H_2 evolution, photoreduction of CO_2 to produce hydrocarbon fuels, etc [128-133]. According to the direct Z-Scheme mechanism, the typical schematic is presented in Figure 6C, which consists of 3 binary Z-scheme systems, including the WO_3-$BiVO_4$, $BiVO_4$-CdS, and CdS-Cu_2O, which are sequentially connected. On the other hand, this system can be considered a typical cascade direct Z-scheme system in which these mentioned above binary direct Z-schemes are consequently connected.

The first Z-scheme system involves WO_3-$BiVO_4$, in which the potential positions of CB-WO_3 (0.56 V) are negative enough to transfer its photoinduced electrons to the VB-$BiVO_4$ (2.73 V), which can be photoexcited to CB-$BiVO_4$ position (0.3 V). The second Z-scheme system can then form, and the VB-$BiVO_4$ photoinduced electrons (0.3 V) can transfer to VB-CdS position (2.18 V), which can be photoexcited to its CB position (-0.28 V) to form the $BiVO_4$-CdS Z-scheme system. The electron transfer from the Cb-CdS (-0.28 V) to VB-Cu_2O (0.2.05 V) and the final photoexcitation to the CB-Cu_2O (-0.36 V) construct the third Z-scheme component. On the other hand, based on the migration of the CB-CdS electrons to the VB-Cu_2O position, the final path of the photoinduced electrons is CB-Cu_2O. These CB-Cu_2O accumulated electrons are more powerful reducing centers (-0.36 V) than the CB- WO_3 accumulated electrons in type II-heterojunction mechanism in the CB-WO_3 position (0.56 V), and capable of producing enough superoxide radicals via the reduction of a high amounts of the dissolved oxygen. These electrons can also directly reduce SFSZ molecules (E: about 0.75 V). As proved by scavenging agents, superoxide radicals can also react with SFSZ molecules, which is the more effective species in its degradation. In this direct Z-scheme mechanism, the holes must be accumulated in VB-WO_3 (3.55 V), which are more powerful oxidizing agents than those collected in the VB-Cu_2O (2.05 V) in the type II-heterojunction system. These accumulated holes can effectively oxidize water to hydroxyl radicals, as the second critical active centers for SFSZ photodegradation based on the results obtained in the scavenging agent study. Based on the results, the successive direct Z-scheme system is suitable for illustrating the SFSZ photodegradation using the proposed quadripartite catalyst.

Reusability of the catalyst: The reusability of the fabricated photocatalyst was kinetically evaluated as a critical economic issue, and the results obtained were illustrated in detail in the first part of the work [79]. After the photodegradation of SFSZ under optimized RSM runs' condition, but under various illumination times, the reused catalyst was washed and dried 100°C for 20 min for the next run. Three reusing runs were performed, and the average vale was obtained each time based on triplicates. Based on the results, typical Hinshelwood plots were constructed, and average slopes of 0.065 ± 0.010, 0.053 ± 0.007, and 0.054 ± 0.004 min^{-1} were calculated for the first to third runs, respectively, as the pesido-first order rate constant, k. To validate the reusability of the catalyst statistically, the statistical 't-test' approach was used based on the pooled standard deviation of 0.008 min^{-1} obtained in three classes of data runs. The smaller calculated t-value of 1.77 than the critical value of $t_{0.05, 4}$= 2.78 [76], proved that there is no considerable difference between the k-values obtained. Thus, the activity of the photocatalyst critically remained after 3 reusing runs at the considered time interval [79]. It is worth mentioning that individual CdS photocatalysts suffer from the photo corrosion effect. Here, this was overcome in the proposed quadripartite photocatalyst, and no leached Cd(II) cations were observed at the end of the photodegradation process, as tested via spot test analysis of the solution against sulfide anions, and no yellow CdS was observed.

Effect of various waters: To test the applicability of the proposed quadripartite photocatalyst for photodegrading SFSZ in various water sources, SFSZ solutions were prepared in different water matrixes like distilled water, pool water (in our university), tap water (in our laboratory), well water (in our university), Zaiandehrood river (Isfahan, Iran), and Zarcheshmeh river (Semirom, Isfahan Iran) and the photodegradation experiments were carried out under the RSM optimal runs' condition. The obtained UV-Vis spectra are compared in Figure 7. As proved by the results, change in the water resource has no considerable effect on the activity of the photocatalyst, meaning that the photocatalyst can be excellently used in various wastewater samples for the successful photodegradation of SFSZ. As the results show, a relatively small change in the obtained C/Co values (inversely, as a measure of the photodegraded SFSZ molecules) was obtained with various water samples concerning the SFSZ solution prepared in distilled water. In these cases, some inorganic species may scavenge some reactive species and slightly decrease the degradation efficiency. In contrast, some inorganic substances may produce reactive radicals that can enhance photodegradation efficiency. It is worth mentioning that no analysis was done on the water samples used, and they were used to prepare SFSZ solutions as received.

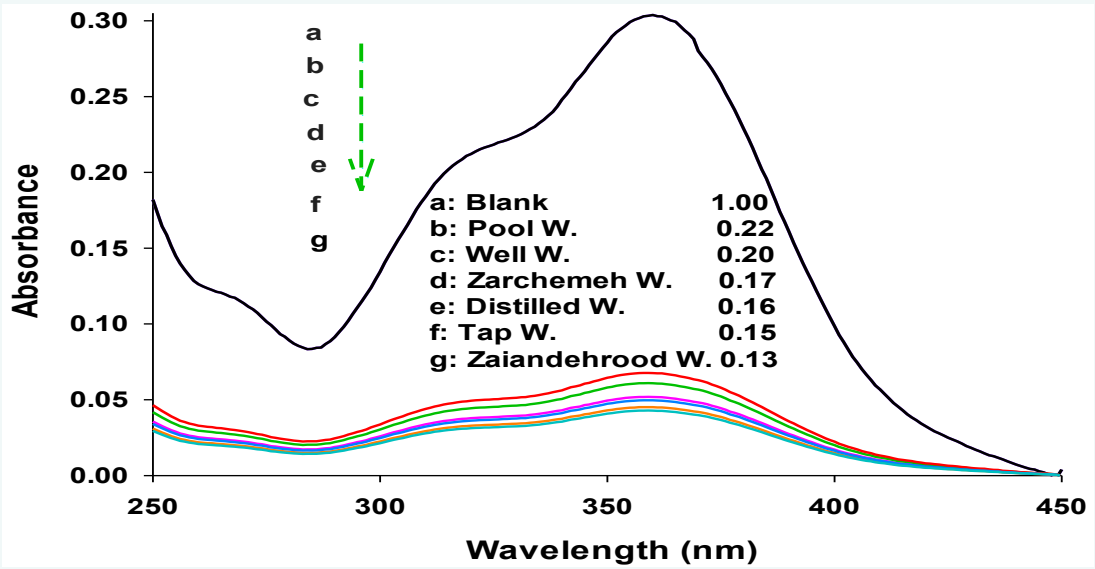

Figure 7: Effects of various waters on SFSZ removal by the proposed catalyst in the conditions of: catalysts dose 0.4 g/L, C_{SFSZ}: 6.25 mg/L, irradiation time: 30 min, pH 9.

ACKNOWLEDGMENT

The authors thank Mohammad Alizadeh and Mohammad Hossein Kazemzadeh for performing instrumental analysis of the samples, as experts in laboratory analysis in Shahreza Branch, Islamic Azad University, Isfahan, Iran. The authors also thank the president of Shahreza Branch, Islamic Azad University, Iran, for supporting this work.

CONCLUSIONS

A synergist photocatalytic activity was achieved for the quadripartite catalyst concerning the individual catalyst and their binary system. This boosted effect can be related to the efficient e/h separation in the quadripartite catalyst that is well described by the direct Z-scheme mechanism, consisting of 3 binary Z-scheme systems sequentially connected. In the first Z-scheme system (WO_3-$BiVO_4$), the potential positions of CB-WO_3 are negative enough to electron transfer to the VB-$BiVO_4$. In the second Z-scheme, electron transfers from the VB-$BiVO_4$ to VB-CdS position. The third Z-scheme system forms between the CdS-Cu_2O, which finally accumulates the electrons in CB-Cu_2O. These CB-Cu_2O electrons are more powerful reducing centers than the CB- WO_3 accumulated electrons in the type II-heterojunction mechanism and can produce enough superoxide radicals. These electrons can also directly reduce SFSZ molecules (E: about 0.75 V). As proved by scavenging agents, superoxide radicals can also react with SFSZ molecules, which are the more effective species. In this direct Z-scheme mechanism, the holes must be accumulated in VB-WO_3 as more powerful oxidizing agents than those of VB-Cu_2O in the type II-heterojunction system. These accumulated holes can effectively oxidize water to hydroxyl radicals as the second critical center for SFSZ photodegradation based on the results obtained in the scavenging agent study. Based on the results, the successive direct Z-scheme system is suitable for illustrating the SFSZ photodegradation using the proposed quadripartite catalyst.

REFERENCES

1. Salman MS, Sheikh MC, Hasan MM, Hasan MN, Kubra KT, Rehan AI, et al. Chitosan-coated cotton fiber composite for efficient toxic dye encapsulation from aqueous media. Appl Surface Sci. 2023; 622: 157008.
2. Kubra KT, Hasan MM, Hasan MN, Salman MS, Khaleque MA, Sheikh MC, et al. The heavy lanthanide of Thulium(III) separation and recovery using specific ligand-based facial composite adsorbent. Colloids Surfaces A: Physicochemical and Engineering Aspects. 2023; 667: 131415.
3. Kubra KT, Salman MS, Hasan MN. Enhanced toxic dye removal from wastewater using biodegradable polymeric natural adsorbent. J Mol Liq, 2021; 328: 115468.
4. Awual MR, Hasan MN, Hasan MM, Salman MS, Sheikh MC, Kubra KT, et al. Green and robust adsorption and recovery of Europium(III) with a mechanism using hybrid donor conjugate materials. Separation Purif Techn. 2023; 319: 124088.
5. Awual MR. Novel nanocomposite materials for efficient and selective mercury ions capturing from wastewater. Chemical Eng J. 2017; 307: 456-465.
6. Awual MR, Hasan MM, Eldesoky GE, Khaleque MA, Rahman MM, Naushad M. Facile mercury detection and removal from aqueous media involving ligand impregnated conjugate nanomaterials. Chemical Eng J. 2016; 290: 243-251.
7. Zheng M, Chen J, Zhang L, Cheng Y, Lu C, Liu Y, et al. Metal organic frameworks as efficient adsorbents for drugs from wastewater. Materials Today Comm. 2022; 31: 103514.
8. Wang J, Rao C, Lu L, Zhang S, Muddassir M, Liu J, Efficient photocatalytic degradation of methyl violet using two new 3D MOFs directed by different carboxylate spacers. Cryst Eng Comm. 2021; 23: 741-747.
9. Wu Y, He X, Wang X, Xv J, Muddassir M, Ansari IA, et al. Synergistic efficacy unleashed: Co/Ni-based catalysts as a versatile powerhouse for photocatalytic degradation of ornidazole. Inorganica Chimica Acta. 2024; 568: 122115.
10. Dong X, Li Y, Li D, Liao D, Qin T, Prakash O, et al. A new 3D 8-connected Cd(ii) MOF as a potent photocatalyst for oxytetracycline antibiotic degradation. Cryst Eng Comm. 2022; 24: 6933-6943.
11. Xiang R, Zhou C, Liu Y, Qin T, Li D, Dong X, et al. A new type Co(II)-based photocatalyst for the nitrofurantoin antibiotic degradation. J Mol Stru. 2024; 1312: 138501.
12. Pugazhenthiran N, Murugesan S, Sathishkumar P, Anandan S. Photocatalytic degradation of ceftiofur sodium in the presence of gold nanoparticles loaded TiO2 under UV–visible light. Chem Eng J. 2014; 241: 401-409.
13. Ji Y, Yang Y, Zhou L, Wang L, Lu J, Ferronato C, et al. Photodegradation of sulfasalazine and its human metabolites in water by UV and UV/peroxydisulfate processes. Water Res. 2018; 133: 299-309.
14. Carolin CF, Kumar PS, Saravanan A, Joshiba GJ, Naushad M. Efficient techniques for the removal of toxic heavy metals from aquatic environment: A review. J Env Chem Eng. 2017; 5: 2782-2799.
15. Awual MR, Hasan MM, Iqbal J, Islam MA, Islam A, Khandaker S, et al. Ligand based sustainable composite material for sensitive nickel(II) capturing in aqueous media. J Env Chem Eng. 2020; 8: 103591.
16. Awual MR, Hasan MM, Asiri AM, Rahman MM. Cleaning the arsenic(V) contaminated water for safe-guarding the public health using novel composite material. Composites Part B: Engin. 2019; 171: 294-301.
17. Kubra KT, Salman MS, Znad H, Hasan MN. Efficient encapsulation of toxic dye from wastewater using biodegradable polymeric adsorbent. J Mol Liquids. 2021; 329: 115541.
18. Waliullah RM, Rehan AI, Awual ME, Rasee AI, Sheikh MC, Salman MS, et al. Optimization of toxic dye removal from contaminated water using chitosan-grafted novel nanocomposite adsorbent. J Mol Liquids. 2023; 388: 122763.
19. Pham TD, Bui TT, Trang Truong TT, Hoang TH, Le TS, Duong VD, et al. Adsorption characteristics of beta-lactam cefixime onto nanosilica fabricated from rice HUSK with surface modification by polyelectrolyte. J Mol Liquids. 2020; 298: 111981.
20. Luhar I, Luhar S, Abdullah MMAB, Razak RA, Vizureanu P, Sandu AV, et al. A State-of-the-Art Review on Innovative Geopolymer Composites Designed for Water and Wastewater Treatment. Materials. 2021; 14: 7456.
21. Rafiq A, Ikram M, Ali S, Niaz F, Khan M, Khan Q, et al. Photocatalytic degradation of dyes using semiconductor photocatalysts to clean industrial water pollution. J Industrial Eng Chem. 2021; 97: 111-128.
22. Soni V, Khosla A, Singh P, Nguyen VH, Le QV, Selvasembian R, et al. Current perspective in metal oxide based photocatalysts for virus disinfection: A review. J Env Management. 2022; 308: 114617.
23. Malhotra M, Sudhaik A, Sonu, Raizada P, Ahamad T, Nguyen VH, et al. An overview on cellulose-supported photocatalytic materials for the efficient removal of toxic dyes. Industrial Crops and Products. 2023; 202: 117000.

24. Ajmal A, Majeed I, Malik RN, Iqbal M, Nadeem MA, Hussain I, et al. Photocatalytic degradation of textile dyes on Cu2O-CuO/TiO2 anatase powders. J Env Chem Eng. 2016; 4: 2138-2146.

25. Rezaee J, Salimi F, Karami C. Removal of Eriochrome Black T dye from water solution using modified nano-boehmite by organic compounds, Desalination and Water Treatment. 2019; 139: 342-351.

26. Hasan I, Alharthi FA. Caffeine-alginate immobilized CeTiO4 bionanocomposite for efficient photocatalytic degradation of methylene blue. J Photochem Photobiology A: Chemistry. 2022; 433: 114126.

27. Rao C, Zhou L, Pan Y, Lu C, Qin X, Sakiyama H, et al. The extra-large calixarene-based MOFs-derived hierarchical composites for photocatalysis of dye: Facile syntheses and contribution of carbon species. J Alloys Compounds. 2022; 897: 163178.

28. Kumar A, Singh P, Khan AAP, Le QV, Nguyen V-H, Thakur S, et al. CO2 photoreduction into solar fuels via vacancy engineered bismuth-based photocatalysts: Selectivity and mechanistic insights. Chem Eng J. 2022; 439: 135563.

29. Meena PL, Surela AK, Chhachhia LK, Meena J, Meena R. Investigation of the photocatalytic potential of C/N-co-doped ZnO nanorods produced via a mechano-thermal process. Nanoscale Advances. 2025; 7: 1335-1352.

30. Meena PL, Poswal K, Surela AK, Saini JK. Synthesis of graphitic carbon nitride/zinc oxide (g-C3N4/ZnO) hybrid nanostructures and investigation of the effect of ZnO on the photodegradation activity of g-C3N4 against the brilliant cresyl blue (BCB) dye under visible light irradiation. Advanced Composites and Hybrid Materials. 2022; 6: 16.

31. Meena PL, Poswal K, Surela AK, Meena KS, Mordhiya B. Ag2O-adorned ZnO nanostructures: cooperative and sustainable nanomaterial system for effective reduction and mineralization of hazardous water pollutants. Env Sci Pollut Res. 2023; 30: 68770-68791.

32. Meena PL, Chhachhia LK, Surela AK. Plant axillary stem gall extract mediated bioengineered CuO nanoprisms as robust and reusable catalyst for photocatalytic and catalytic degradation of water pollutants. J Mol Stru. 2024; 1303: 137575.

33. Nam W, Woo K, Han G. Photooxidation of anionic surfactant (sodium lauryl sulfate) in a three-phase fluidized bed reactor using TiO2/SiO2 photocatalyst. J Indust Engin Chem. 2009; 15: 348-353.

34. Ciğeroğlu Z, Şahin S, Kazan ES. One-pot green preparation of deep eutectic solvent-assisted ZnO/GO nanocomposite for cefixime trihydrate photocatalytic degradation under UV-A irradiation. Biomass Conversion and Biorefinery. 2022; 12: 73-86.

35. Esmaili Z, Solaimany Nazar AR, Farhadian M. Degradation of furfural in contaminated water by titanium and iron oxide nanophotocatalysts based on the natural zeolite (clinoptilolite). Scientia Iranica. 2017; 24: 1221-1229.

36. Ye D, Liu L, Peng Q, Qiu J, Gong H, Zhong A, et al. Effect of Controlling Thiophene Rings on D-A Polymer Photocatalysts Accessed via Direct Arylation for Hydrogen Production. Molecules. 2023; 28: 4507.

37. AlSalhi MS, Sakthisabarimoorthi A, Devanesan S, Martin Britto Dhas SA, Jose M. Study on photocatalytic and impedance spectroscopy investigations of composite CuO/ZnO nanoparticles. J Materials Sci. 2019; 30: 13708-13718.

38. EL Bekkali C, Bouyarmane H, Laasri S, Laghzizil A, Saoiabi A. Effects of metal oxide catalysts on the photodegradation of antibiotics effluent. Iranian. J Catalysis. 2018; 8: 241-247.

39. Meena PL, Chhachhia LK, Surela AK. Synthesis of phytogenically deposed Ag nanospheres on ZnO nanosheets for photocatalytic and catalytic applications. Optical Materials. 2024; 148: 114916.

40. Ahmad N, Anae J, Khan MZ, Sabir S, Yang XJ, Thakur VK, et al. Visible light-conducting polymer nanocomposites as efficient photocatalysts for the treatment of organic pollutants in wastewater. J Env Manag. 2021; 295: 113362.

41. da Silva WL, Druzian DM, Oviedo LR, Muraro PCL, Oviedo VR. Silver Nanoparticles for Photocatalysis and Biomedical Applications, Silver Micro-Nanoparticles-Properties, Synthesis, Characterization, and Applications. IntechOpen. 2021.

42. Eslami A, Oghazyan A, Sarafraz M. Magnetically separable MgFe2O4 nanoparticle for efficient catalytic ozonation of organic pollutants. Iranian J Catalysis. 2018; 8: 95-102.

43. Zebardast M, Shojaei AF, Tabatabaeian K. Enhanced removal of methylene blue dye by bimetallic nano-sized MOF-5s. Iranian J Catalysis. 2018; 8: 297-309.

44. Kangralkar MV, Jayappa M. Green synthesis of iron nanoparticles by Terminalia arjuna bark extract and photodegradation of rose bengal. Iranian J Catalysis. 2020; 10: 181-188.

45. Yaghoubi-berijani M, Bahramian B, Zargari S, The study of photocatalytic degradation mechanism under visible light irradiation on BiOBr/Ag nanocomposite. Iranian J Catalysis. 2020; 10: 307-317.

46. Karami A, Monsef R, Waleed I, Kareem HL, Ibrahim IT, Salavati-Niasari M. Microwave synthesized erbium vanadate nano-photocatalyst: Application for enhanced degradation of contaminated water. Int J Hydr Energ. 2023; 48: 8499-8513.

47. Panahi A, Monsef R, Hussein SA, Hammood SA, Al-Azzawi WK, Raffik DE, et al. Multidisciplinary methods for synthesis of visible-light-driven TmVO4 nanostructure photocatalyst with enhanced photocatalytic activity towards removal of toxic contaminates. Int J Hydro Energ. 2023; 48: 33155-33165.

48. Meena PL, Poswal K, Surela AK, Saini JK. Synthesis of g-C3N4/ZnO nanostructures via mechano-thermal method for photocatalytic degradation of methylene blue dye. Int J Env Sci Techn. 2024; 22: 833-848.

49. Nguyen Phuoc H, Le QT, Pham TC-T, Le TT. Synthesis of Glue-Free NaA Zeolite Granules from Natural Kaolin for the Adsorption of Pb(II) Ions in Aqueous Solution Using a Fixed-Bed Column Study. ACS Omega. 2021; 6: 21024-21032.

50. Tehubijuluw H, Subagyo R, Kusumawati Y, Prasetyoko D. The impregnation of ZnO onto ZSM-5 derived from red mud for photocatalytic degradation of methylene blue. Sustainable Env Res. 2022; 32: 4.

51. Rahman ROA, El-Kamash AM, Hung YT. Applications of Nano-Zeolite in Wastewater Treatment: An Overview. Water. 2022; 14: 137.

52. Singh A, Singh AK, Liu J, Kumar A, Syntheses, design strategies, and photocatalytic charge dynamics of metal–organic frameworks (MOFs): a catalyzed photo-degradation approach towards organic dyes. Catal Sci Technol. 2021; 11: 3946-3989.

53. Piriyanon J, Chankhanittha T, Youngme S, Hemavibool K, Nijpanich S, Juabrum S, et al. Fabrication of MoS2/Ag3PO4 S-scheme photocatalyst for visible-light-active degradation of organic dye and antibiotic in wastewater. J Mat Sci. 2021; 32: 19798-19819.

54. AttariKhasraghi N, Zare K, Mehrizad A, Modirshahla N, Behnajady MA. Achieving the Enhanced Photocatalytic Degradation of Ceftriaxone Sodium Using CdS-g-C3N4 Nanocomposite under Visible Light Irradiation: RSM Modeling and Optimization. J Inorg Organometallic Polym Mater. 2021; 31: 3164-3174.

55. Gulino A, Papanikolaou G, Lanzafame P, Aaliti A, Primerano P, Spitaleri L, et al. Synthesis, Characterization and Photocatalytic Behavior of SiO2@nitrized-TiO2 Nanocomposites Obtained by a Straightforward Novel Approach. Chem Open. 2021; 10: 1033-1040.

56. Adenuga D, Skosana S, Tichapondwa S, Chirwa E. Synthesis of a plasmonic AgCl and oxygen-rich Bi24O31Cl10 composite heterogeneous catalyst for enhanced degradation of tetracycline and 2,4-dichlorophenoxy acetic acid. RSC Adv. 2021; 11: 36760-36768.

57. Sun K, Zhan G, Chen H, Lin S. Low-Operating-Temperature NO2 Sensor Based on a CeO2/ZnO Heterojunction. Sensors (Basel). 2021; 21: 8269.

58. Sharma K, Sudhaik A, Raizada P, Thakur P, Pham XM, Van Le Q, et al. Constructing α-Fe2O3/g-C3N4/SiO2 S-scheme-based heterostructure for photo-Fenton like degradation of rhodamine B dye in aqueous solution. Env Sci Pollut Res Int. 2023; 30: 124902-124920.

59. Kumar N, Kumari M, Ismael M, Tahir M, Sharma RK, Kumari K, et al. Graphitic carbon nitride (g-C3N4)-assisted materials for the detection and remediation of hazardous gases and VOCs. Environ Res. 2023; 231: 116149.

60. Dhull P, Sudhaik A, Sharma V, Raizada P, Hasija V, Gupta N, et al. An overview on InVO4-based photocatalysts: Electronic properties, synthesis, enhancement strategies, and photocatalytic applications. Molecular Catalysis. 2023; 539: 113013.

61. Rostami-Vartooni A, Moradi-Saadatmand A, Bagherzadeh M, Mahdavi M. Green synthesis of Ag/Fe3O4/ZrO2 nanocomposite using aqueous Centaurea cyanus flower extract and its catalytic application for reduction of organic pollutants. Iranian J Catalysis. 2019; 9: 27-35.

62. Sobhani-Nasab A, Eghbali-Arani M, Hosseinpour-Mashkani SM, Ahmadi F, Rahimi-Nasrabadi M, Ameri V. Eco-friendly preparation and characterization of CuMn2O4 nanoparticles with the green capping agent and their photocatalytic and photovoltaic applications. Iranian J Catalysis. 2020; 10: 91-99.

63. Samandari M, Taghva Manesh A, Hosseini SA, Mansouri S. Process Optimization and Kinetic study of Wet Peroxide Oxidation of Phenol in Wastewater over Mg-Al Nano Mixed Oxide. Iranian J Catalysis. 2021; 11: 175-180.

64. Meena PL, Poswal K, Surela AK, Saini JK. Facile synthesis of ZnO/CuO/Ag2O ternary metal oxide nanocomposite for effective photodegradation of organic water pollutants. Water Sci Technol. 2021; 84: 2615-2634.

65. Alamro FS, Mostafa AM, Abu Al-Ola KA, Ahmed HA, Toghan A. Synthesis of Ag Nanoparticles-Decorated CNTs via Laser Ablation Method for the Enhancement the Photocatalytic Removal of Naphthalene from Water. Nanomaterials (Basel). 2021; 11: 2142.

66. Manda AA , Elsayed KA, Gaya UI, Haladu SA, Ercan I, Ercan F, et al. Enhanced photocatalytic degradation of methylene blue by nanocomposites prepared by laser ablation of Bi on CNT-α-Fe2O3 nanoparticles. Optics Laser Technology. 2022; 155: 108430.

67. Isai KA, Shrivatava VS. Photocatalytic degradation of methyl orange using ZnO and Fe doped ZnO: A comparative study. Iranian J Catalysis. 2019; 9: 259-268.

68. Islam A, Teo SH, Islam MT, Mondal AH, Mahmud H, Ahmed S, et al. Harnessing visible light for sustainable biodiesel production with Ni/Si/MgO photocatalyst. Renewable and Sustainable Energy Rev. 2025; 208: 115033.

69. Sharma K, Kumar A, Ahamad T, Le QV, Raizada P, Singh A, et al. Sulphur vacancy defects engineered metal sulfides for amended photo(electro)catalytic water splitting: A review. J Materials Sci Technol. 2023; 152: 50-64.

70. Sharma K, Sonu S, Sudhaik A, Ahamad T, Kaya S, Thakur S, et al. Mechanistic insights into the reaction pathway for efficient cationic dye photocatalytic degradation and the importance of the enhanced charge isolation over dual Z-scheme CeO2/BiOCl/Ag2WO4 photocatalyst. J Water Process Engineering. 2024; 66: 105918.

71. Hasija V, Parwaz Khan AA, Sonu, Katin KP, Kaya S, Singh P, et al. Dual S-scheme Bi2MoO6/g-C3N4/Ag2MoO4 ternary heterojunction: Interfacial charge transfer, broadband spectrum, enhanced redox ability. Solid State Sci. 2024; 157: 107693.

72. Rana A, Sonu A, Sudhaik A, Chawla A, Raizada P, Kaushik AK, et al. Integrating BiOI/g-C3N4/Bi2WO6 Derived Dual S-Scheme Photocatalyst with Biochar for Emerging Adsorption for Photocatalysis: Multicharge Migration and Mechanistic Insights. Industrial Eng Chem Res. 2024; 63; 6960-6973.

73. Chang JP, Wang CY, Hsu YJ, Wang CY. Cu2O/UiO-66-NH2 composite photocatalysts for efficient hydrogen production from ammonia borane hydrolysis. Appl Catalysis A. 2023; 650: 119005.

74. Obregón S, Caballero A, Colón G. Hydrothermal synthesis of BiVO4: Structural and morphological influence on the photocatalytic activity. Appl Catalysis B. 2012; 117-118: 59-66.

75. Lai HF, Chen CC, Chang YK, Lu CS, Wu RJ. Efficient photocatalytic degradation of thiobencarb over BiVO4 driven by visible light: Parameter and reaction pathway investigations. Separation and Purification Technology. 2014; 122: 78-86.

76. Dunkle SS, Helmich RJ, Suslick KS. BiVO4 as a Visible-Light Photocatalyst Prepared by Ultrasonic Spray Pyrolysis. J Phys Chem C. 2009; 113: 11980-11983.

77. Aguilera-Ruiz E, García-Pérez UM, de la Garza-Galván M, Zambrano-Robledo P, Bermúdez-Reyes B, Peral J. Efficiency of Cu2O/BiVO4 particles prepared with a new soft procedure on the degradation of dyes under visible-light irradiation. Appl Surface Sci. 2015; 328: 361-367.

78. Selvarajan S, Suganthi A, Rajarajan M, Arunprasath K. Highly efficient BiVO4/WO3 nanocomposite towards superior photocatalytic performance. Powder Technology. 2017; 307: 203-212.

79. Omrani N, Nezamzadeh-Ejhieh A. A novel quadripartite Cu2O-CdS-BiVO4-WO3 visible-light driven photocatalyst: Brief characterization and study the kinetic of the photodegradation and mineralization of sulfasalazine. J Photochem Photobiol. 2020; 400: 112726.

80. Arshadi-Rastabi S, Moghaddam J, Reza Eskandarian M. Synthesis, characterization and stability of Cu2O nanoparticles produced via supersaturation method considering operational parameters effect. J Industrial Eng Chem. 2015; 22: 34-40.

81. Qutub N, Pirzada BM, Umar K, Sabir S. Synthesis of CdS nanoparticles using different sulfide ion precursors: Formation mechanism and photocatalytic degradation of Acid Blue-29. J Env Chem Eng. 2016; 4: 808-817.

82. Martínez-de la Cruz A, Pérez UMG. Photocatalytic properties of BiVO4 prepared by the co-precipitation method: Degradation of

rhodamine B and possible reaction mechanisms under visible irradiation. Materials Res Bull. 2010; 45: 135-141.

83. Omrani N, Nezamzadeh-Ejhieh A. A ternary Cu2O/BiVO4/WO3 nano-composite: Scavenging agents and the mechanism pathways in the photodegradation of sulfasalazine. J Mol Liquids. 2020; 315: 113701.

84. Omrani N, Nezamzadeh-Ejhieh A. BiVO4/WO3 nano-composite: characterization and designing the experiments in photodegradation of sulfasalazine. Env Sci Pollut Res Int. 2020; 27: 44292-44305.

85. Omrani N, Nezamzadeh-Ejhieh A. Photodegradation of sulfasalazine over Cu2O-BiVO4-WO3 nano-composite: Characterization and experimental design. Int J Hydrogen Energy. 2020; 45: 19144-19162.

86. Omrani N, Nezamzadeh-Ejhie A. A comprehensive study on the mechanism pathways and scavenging agents in the photocatalytic activity of BiVO4/WO3 nano-composite. J Water Process Engineering. 2020; 33; 101094.

87. Omrani N, Nezamzadeh-Ejhieh A. Focus on scavengers' effects and GC-MASS analysis of photodegradation intermediates of sulfasalazine by Cu2O/CdS nanocomposite. Separation Purification Technol. 2020; 235: 116228.

88. Omrania N, Nezamzadeh-Ejhieha A, Alizadehb M. Brief study on the kinetic aspect of photodegradation of sulfasalazine aqueous solution by cuprous oxide/cadmium sulfide nanoparticles. Catalyst. 2019; 17: 24.

89. Rodríguez P, Muñoz-Aguirre N, Martínez ESM, Gonzalez G, Zelaya O, Mendoza J. Formation of CdS nanoparticles using starch as capping agent. Appl Surface Sci. 2008; 255: 740-742.

90. Amiri M, Pardakhti A, Ahmadi-Zeidabadi M, Akbari A, Salavati-Niasari M. Magnetic nickel ferrite nanoparticles: Green synthesis by Urtica and therapeutic effect of frequency magnetic field on creating cytotoxic response in neural cell lines. Colloids and Surfaces B: Biointerfaces. 2018; 172: 244-253.

91. El Bouraie M, Ibrahim S. Differentiation Between Metronidazole Residues Disposal by Using Adsorption and Photodegradation Processes Onto MgO Nanoparticles. Int J Nanomed. 2020; 15: 7117-1141.

92. Seyedi-Chokanlou T, Aghabeygi S, Molahasani N, Abrinaei F. Applying Taguchi method to optimize the synthesis conditions of ZrO2/TiO2/ZnO nanocomposite for high-performance photodegradation of Congo red. Iranian J Catalysis. 2021; 11: 9-58.

93. Manikandan B, Murali K, John R. Optical, morphological and microstructural investigation of TiO2 nanoparticles for photocatalytic application. Iranian J Catalysis. 2021; 11: 1-11.

94. Arunkumar M, Samson Nesaraj A. Photocatalytic degradation of malachite green dye using NiAl2O4 and Co doped NiAl2O4 nanophotocatalysts prepared by simple one pot wet chemical synthetic route. Iranian J Catalysis. 2020; 10: 235-245.

95. Manikandan Balakrishnan RJ. Properties of sol-gel synthesized multiphase TiO2 (AB)-ZnO (ZW) semiconductor nanostructure: an effective catalyst for methylene blue dye degradation. Iranian J Catalysis. 2020; 10: 1-16.

96. Salavati-Niasari M, Salemi P, Davar F. Oxidation of cyclohexene with tert-butylhydroperoxide and hydrogen peroxide catalysted by Cu(II), Ni(II), Co(II) and Mn(II) complexes of N,N′-bis-(α-methylsalicylidene)-2,2-dimethylpropane-1,3-diamine, supported on alumina. J Mol Catalysis. 2005; 238: 215-222.

97. Mazloom F, Masjedi-Arani M, Ghiyasiyan-Arani M, Salavati-Niasari M. Novel sodium dodecyl sulfate-assisted synthesis of Zn3V2O8 nanostructures via a simple route. J Mol Liquids. 2016; 214: 46-53.

98. Landi S, Segundo IR, Freitas E, Vasilevskiy M, Carneiro J, Tavares CJ. Use and misuse of the Kubelka-Munk function to obtain the band gap energy from diffuse reflectance measurements. Solid State Commun. 2022; 341: 114573.

99. Suram SK, Newhouse PF, Gregoire JM. High Throughput Light Absorber Discovery, Part 1: An Algorithm for Automated Tauc Analysis. ACS Comb. Sci. 2016; 18: 673-681.

100. Shaterian M, Enhessari M, Rabbani D, Asghari M, Salavati-Niasari M. Synthesis, characterization and photocatalytic activity of LaMnO3 nanoparticles. Appl Surface Sci. 2014; 318: 213-217.

101. Norouzzadeh P, Mabhouti K, Golzan M, Naderali R. Investigation of structural, morphological and optical characteristics of Mn substituted Al-doped ZnO NPs: a Urbach energy and Kramers-Kronig study. Optik. 2020; 204: 164227.

102. Makuła P, Pacia M, Macyk W. How To Correctly Determine the Band Gap Energy of Modified Semiconductor Photocatalysts Based on UV–Vis Spectra. J Phys Chem Lett. 2018; 9: 6814-6817.

103. Tauc J. Chap. 5 of" Optical Properties of Solids" ed. By F. Abeles. North-Holland Publishing Company. Amsterdam. 1972.

104. Coulter JB, Birnie III DP. Assessing Tauc Plot Slope Quantification: ZnO Thin Films as a Model System. physica status solii (b). 2018; 255: 1700393.

105. Köferstein R, Jäger L, Ebbinghaus SG. Magnetic and optical investigations on LaFeO3 powders with different particle sizes and corresponding ceramics. Solid State Ionics. 2013; 249-250: 1-5.

106. Köferstein R, Ebbinghaus SG. Investigations of BaFe0.5Nb0.5O3 nano powders prepared by a low temperature aqueous synthesis and resulting ceramics. J Eur Ceram Soc. 2017; 37: 1509-1516.

107. Katsumata KI, Motoyoshi R, Matsushita N, Okada K. Preparation of graphitic carbon nitride (g-C3N4)/WO3 composites and enhanced visible-light-driven photodegradation of acetaldehyde gas. J Hazard Mater. 2013; 260: 475-482.

108. Che H, Che G, Jiang E, Liu C, Dong H, Li C. A novel Z-Scheme CdS/Bi3O4Cl heterostructure for photocatalytic degradation of antibiotics: Mineralization activity, degradation pathways and mechanism insight. J Taiwan Inst Chem Engineers. 2018; 91: 224-234.

109. Dianat S. Visible light induced photocatalytic degradation of direct red 23 and direct brown 166 by InVO4-TiO2 nanocomposite. Iranian J Catal. 2018; 8: 121-132.

110. Muhammad S, Hussain ST, Waseem M, Naeem A, Hussain J, Tariq Jan M. Surface charge properties of zirconium dioxide. Iranian J Sci Techn (Sciences). 2012; 36: 481-486.

111. Emara MM, Ali SH, Hassan AA, Kassem TSE, Van Patten PG. How does photocatalytic activity depend on adsorption, composition, and other key factors in mixed metal oxide nanocomposites?. Colloid and Interface Science Communications. 2021; 40: 100341.

112. Tsao CW, Fang MJ, Hsu YJ. Modulation of interfacial charge dynamics of semiconductor heterostructures for advanced photocatalytic applications. Coordination Chem Rev. 2021; 438: 213876.

113. Yousefzadeh S, Matin AR, Ahmadi E, Sabeti Z, Alimohammadi M, Aslani H, et al. Response surface methodology as a tool for modeling and optimization of Bacillus subtilis spores inactivation by UV/nano-Fe0 process for safe water production. Food Chem Toxicol. 2018; 114: 334-345.

114. Najafian N, Aarabi A, Nezamzadeh-Ejhieh A, Intensified Phycobiliprotein Extraction from Spirulina Platensis by Freezing and Ultrasound Methods. Iranian J Chem Chem Eng. 2023; 42: 601-617.

115. Khangah AH, Sarraf MJ, Ale Ebrahim H, Tabatabaee M. Synthesis of ternary Ce2O3/La2O3/Fe3O4 oxides as a potential catalyst for SO2 reduction by CH4 to sulphur. Iranian J Catalysis. 2020; 10: 135-148.

116. Salavati H, Teimouri A, Kazemi S. Developments of modified magnetic nanoparticle-supported heteropolyacid catalytic performances in dibenzothiophene desulfurization. Iranian J Catalysis. 2017; 7: 303-315.

117. Massoudinejad M, Sadani M, Gholami Z, Rahmati Z, Javaheri M, Keramati H, et al. Optimization and modeling of photocatalytic degradation of Direct Blue 71 from contaminated water by TiO2 nanoparticles: Response surface methodology approach (RSM). Iranian J Catalysis. 2019; 9: 121-132.

118. Parsafard N. Optimization of main parameters affecting activity and octane number produced from catalytic isomerization of n-heptane using response surface methodology. Iranian J Catalysis. 2023; 13: 125-133.

119. Govindan K, Chandran HT, Raja M, Maheswari SU, Rangarajan M. Electron scavenger-assisted photocatalytic degradation of amido black 10B dye with Mn3O4 nanotubes: A response surface methodology study with central composite design. J Photochem Photobiol. 2017; 341: 146-156.

120. Vione D, Khanra S, Man SC, Maddigapu PR, Das R, Arsene C, et al. Inhibition vs. enhancement of the nitrate-induced phototransformation of organic substrates by the •OH scavengers bicarbonate and carbonate. Water Res. 2009; 43: 4718-4728.

121. Tan T, Beydoun D, Amal R. Effects of organic hole scavengers on the photocatalytic reduction of selenium anions. J Photochem Photobiol. 2003; 159: 273-280.

122. Sapper H, Kang SO, Paul HH, Lohmann W. The reversibility of the vitamin C redox system: electrochemical reasons and biological aspects. Z Naturforsch C Biosci. 1982; 37: 942-946.

123. Nandi A, Chatterjee LB. Scavenging of superoxide radical by ascorbic acid. J Biosci. 1987; 11: 435-441.

124. Xu Q, Zhang L, Yu J, Wageh S, Al-Ghamdi AA, Jaroniec M. Direct Z-scheme photocatalysts: Principles, synthesis, and applications. Materials Today. 2018; 21: 1042-1063.

125. Pu YC, Lin WH, Hsu YJ. Modulation of charge carrier dynamics of NaxH2−xTi3O7-Au-Cu2O Z-scheme nanoheterostructures through size effect. Appl Catalysis. 2015; 163: 343-351.

126. Li JM, Tsao CW, Fang MJ, Chen CC, Liu CW, Hsu YJ. TiO2-Au-Cu2O Photocathodes: Au-Mediated Z-Scheme Charge Transfer for Efficient Solar-Driven Photoelectrochemical Reduction. ACS Applied Nano Materials. 2018; 1: 6843-6853.

127. Buoro RM, Diculescu VC, Lopes IC, Serrano SHP, Oliveira-Brett AM. Electrochemical Oxidation of Sulfasalazine at a Glassy Carbon Electrode. Electroanalysis. 2014; 26: 924-930.

128. Dutta V, Sonu S, Raizada P, Thakur VK, Ahamad T, Thakur S. Prism-like integrated Bi(2)WO(6) with Ag-CuBi(2)O(4) on carbon nanotubes (CNTs) as an efficient and robust S-scheme interfacial charge transfer photocatalyst for the removal of organic pollutants from wastewater. Environ Sci Pollut Res Int. 2023; 30: 124530-124545.

129. Sharma K, Hasija V, Malhotra M, Verma PK, Parwaz Khan AA, Thakur S. A review of CdS-based S-scheme for photocatalytic water splitting: Synthetic strategy and identification techniques. Int J Hydrogen Energy. 2024; 52: 804-818.

130. Kumar Y, Sudhaik A, Sharma K, Sonu, Raizada P, Aslam Parwaz Khan A. Construction of magnetically separable novel arrow down dual S-scheme ZnIn2S4/BiOCl/FeVO4 heterojunction for improved photocatalytic activity. J Photochem Photobiol A. 2022; 435: 114326.

131. Malhotra M, Poonia K, Singh P, Khan AAP, Thakur P, Van Le Q, et al. An overview of improving photocatalytic activity of MnO2 via the Z-scheme approach for environmental and energy applications. J Taiwan Institute of Chemical Engineers. 2023; 158: 104945.

132. Parwaz Khan AA, Singh P, Raizada P, Khan A, Asiri AM, Alotaibi MM. Photo-Fenton assisted AgCl and P-doped g-C3N4 Z-scheme photocatalyst coupled with Fe3O4/H2O2 system for 2, 4-dimethylphenol degradation. Chemosphere. 2023; 316: 137839.

133. Kumar A, Singh P, Nguyen VH, Van Le Q, Ahamad T, Thakur S, et al. Rationally constructed synergy between dual-vacancies and Z-scheme heterostructured MoS2-x/g-C3N4/Ca-α-Fe2O3 for high-performance photodegradation of sulfamethoxazole antibiotic from aqueous solution. Chem Eng J. 2023; 474: 145720.

134. Makuła P, Pacia M, Macyk W. How To Correctly Determine the Band Gap Energy of Modified Semiconductor Photocatalysts Based on UV–Vis Spectra. J Phys Chem Lett. 2018; 9: 6814-6817.

135. Coulter JB, Birnie III DP. Assessing Tauc Plot Slope Quantification: ZnO Thin Films as a Model System. Phys Status Solidi B. 2018; 255: 1700393.